



Synergic Evolution of Microstructure-Texture-Stored Energy in Rare-Earth-Added Interstitial-Free Steels Undergoing Static Recrystallization

Peng Liu^{1,2} · Xiaodong Hou³ · Chaoyun Yang¹ · Yikun Luan^{1,2} · Chengwu Zheng^{1,2} · Dianzhong Li^{1,2}

Received: 11 August 2022 / Revised: 30 August 2022 / Accepted: 1 September 2022 / Published online: 3 December 2022
© The Chinese Society for Metals (CSM) and Springer-Verlag GmbH Germany, part of Springer Nature 2022

Abstract

Synergic evolution of microstructure-texture-stored energy in interstitial-free (IF) steels has been investigated to elaborate the effect of dissolved rare-earth (RE) elements on static recrystallization. Grain size, texture fraction and geometrically necessary dislocation distribution of IF steel samples annealed for different times were compared, suggesting that RE elements could postpone recrystallization nucleation but accelerate grain coarsening. The visco-plastic self-consistent model was primarily adopted and verified, then used to calculate the relative activities of different slip systems. It was proved that the compatible deformation of IF steels was very sensitive to dissolved RE elements, in particular the $\{110\}_6\langle 111 \rangle_2$ slip systems became extremely inactive, leading to an α -fibre textures rich configuration of RE-IF steels. Although both IF steels have the same stored energy sequence of which γ -fibre takes precedence in nucleation followed by α -fibre, the nucleation rates of α/γ -fibres driven by the reduced stored energy slowed down in RE-IF steels. Further nucleation-path analyses revealed that shear bands within γ -fibre mainly sacrificed for grain nucleation of $\{111\}\langle 110 \rangle$ orientation, while α -fibre especially prior grain boundaries therein preferred supplying nucleation sites for $\{554\}\langle 225 \rangle$ grains, which accounting for the competitive growth of γ -fibre textures in RE-IF steels rather than being dominated by a single orientation. After grain growth, the major texture of Normal-IF steels had been transferred to $\{554\}\langle 225 \rangle$ from $\{111\}\langle 110 \rangle$, while $\{554\}\langle 225 \rangle$ in RE-IF steels still inherited the orientation advantage and grew up rapidly, thus inducing the grain coarsening. As this work offers a significant understanding of RE microalloying effect on static recrystallization, it will provide references for alloy design and industrial application of IF steels.

Keywords Static recrystallization · IF steels · RE elements · Texture · Grain coarsening · Slip systems

1 Introduction

Interstitial-free (IF) steels have been widely used in automotive and appliance industries due to its superior formability without strain ageing problem, satisfying the requirements of lightweight for parts of complicated shapes. Many investigations have been carried out to study the combined influence of microstructure and crystallographic texture on the overall mechanical performance of IF steels, which suggests that the heterogeneous microstructure with distinct strain-localization can play important roles in oriented nucleation of various textures [1–5]. It was further proved that these locally distorted microstructures (e.g., shear bands [3, 4], dislocation entanglements and dislocation cells [1, 2, 6]) could provide abundant nucleation sites for grains of desirable $\langle 111 \rangle // ND$ orientations [1–3] with excellent deformation resistance, while limiting the appearance of unfavourable $\langle 110 \rangle // RD$ orientations related to planar isotropy

Available online at <http://link.springer.com/journal/40195>.

✉ Yikun Luan
ykluan@imr.ac.cn

✉ Dianzhong Li
dzli@imr.ac.cn

¹ Shenyang National Laboratory for Materials Science, Institute of Metal Research, Chinese Academy of Sciences, Shenyang 110016, China

² School of Materials Science and Engineering, University of Science and Technology of China, Shenyang 110016, China

³ Centre of Excellence for Advanced Materials, Dongguan 523808, China

deterioration [4]. Therefore, it is believed that the excellent formability of IF steels is mainly dominated by the formation of $\{111\}\langle uvw \rangle$ textures, which can be introduced by carefully designed thermomechanical processing, e.g. cold-rolling followed by proper heat treatments.

Inhomogeneous deformation strain and stored energy accumulated in elongated grains of cold-rolled polycrystalline materials can play important roles in microstructure evolution, causing distinct recrystallization kinetics of annealing process [7, 8]. The finishing temperature of intercritical rolling is critical in determining dislocations pile-up and textures configuration: the nucleation mechanism of new grains would shift from strain-induced boundary migration at high finishing temperature to subgrain coalescence at low finishing temperature. The later could produce abundant textures more favourable for drawability [9], similar to the warm rolling executed in a lower temperature range [2]. Inspired by this, temper rolling [10] is further used as the final manufacturing procedure of IF steels, to introduce the inhomogeneous distribution of residual strain desired for texture nucleation. Besides rolling temperature, cold reduction can also enhance strain gradients leading to the γ -fibre intensity increase in IF steels. Severe plastic deformation is another mechanism often used to introduce high dislocation density, which can promote the formation of grains of nanosize to sub-micro-size and desirable orientations after annealing [11, 12]. Furthermore, laminated IF steels [13, 14] with homogeneous layers and lamella structures were also designed and fabricated, showing improved uniform elongation without compromising its strength. These studies are based on the same idea of synergic regulation that deformed microstructure as the precursor can provide more nucleation sites for the grains with preferred textures desired for better mechanical performance.

Meanwhile, other research groups focus on adjusting chemical composition and even steel slag systems to improve IF steel mechanical properties. De Paepe et al. [15] found that stoichiometric ratio $[\text{Ti}^*/\text{C}] \geq 5.9$ of classical Ti-IF grades or $[\text{Ti} \geq 0.025 \text{ wt\%}, \text{Nb} \geq 0.035 \text{ wt\%}]$ of co-alloyed IF steels could achieve complete stabilization of solute carbon in the austenitic temperature region and obtain sufficient strain in finishing train at lower rolling temperature, contributing to the outstanding deep drawing performance. It was also found that lacking of carbide-forming elements, e.g. Nb, V or Ti, would trigger the formation of Lüders bands related to surface wrinkle in stamping process [16]. There are other elements commonly used in IF steels: active Al elements are used to raise steel cleanliness through deoxidation reaction and co-addition of P, Si and Mn multi-elements can offer combined strengthening for steel matrices, but AlN and FeTiP precipitates would increase with raising Al [17] and P [18] content, the former would promote the heat-treated microstructure become equiaxed and homogeneous, while the latter could deteriorate $\{111\}\langle uvw \rangle$ textures and even formability.

Recently, more studies were carried out to explore the roles of RE elements in commercial steels [19–22]; in particular, their modification and purification effects on various inclusions and molten steels, respectively. This approach was adopted into manufacturing of IF steels [23], and it was found that dissolved RE elements could affect the recrystallization kinetics as well. However, these efforts were mainly focused on the effect of RE elements on recrystallization behaviours during hot rolling or among rolling passes, with limited attention to their influences on static recrystallization of cold-rolled sheets subjected to continuous annealing (CA) while minimizing the influence of microstructure characteristics inherited from the early hot-rolling process. Furthermore, the underlying micro-alloying effect of RE elements on microstructure evolution, texture transformation and stored energy partition are still not clear.

The aim of this study is to clarify the mechanism of dissolved RE elements on static recrystallization of IF steels. IF steel samples with and without RE elements were carefully prepared with desired initial microstructure and texture, mechanically rolled and then annealed for varying times to investigate the microstructure evolution, texture transformation, stored energy partition as well as their internal relationships. Efforts were focused on the following three key points: (i) the activation of slip systems and its response to deformation texture formation, (ii) stored energy partition among deformation textures and the resultant nucleation sequence, and (iii) the oriented nucleation and selective growth of recrystallization textures.

2 Experimental

IF steel samples with and without RE elements, named as the RE-IF steel and the Normal-IF steel, respectively, were prepared via vacuum induction melting under laboratory conditions. The La–Ce mischmetal with mass ratio of around 1:2 was added into molten steels after alloying to introduce the desired RE elements. The whole production process and heat treatment schedule are shown in Fig. 1a, b, and the chemical compositions of investigated IF steels are listed in Table 1. The ingots obtained after descaling were completely austenitized at 1200 °C for 2 h to eliminate segregation, forged into square billets of 50 mm thickness and then air-cooled to ambient temperature. These billets were further hot-rolled at austenitic temperature range (1100–930 °C) to obtain hot strips of 5 mm thickness by reversing rolling mill within 7 passes. For a traditional production process (i.e., Route 1), the hot-rolled IF steel strips after pickling would be directly cold-rolled to reduce thickness by 80% reduction with lubrication, followed by CA in which steel samples are heated to 860 °C for 3 min by a rapid thermal processing (RTP-1100) furnace. In this study, however, an additional pre-annealing process

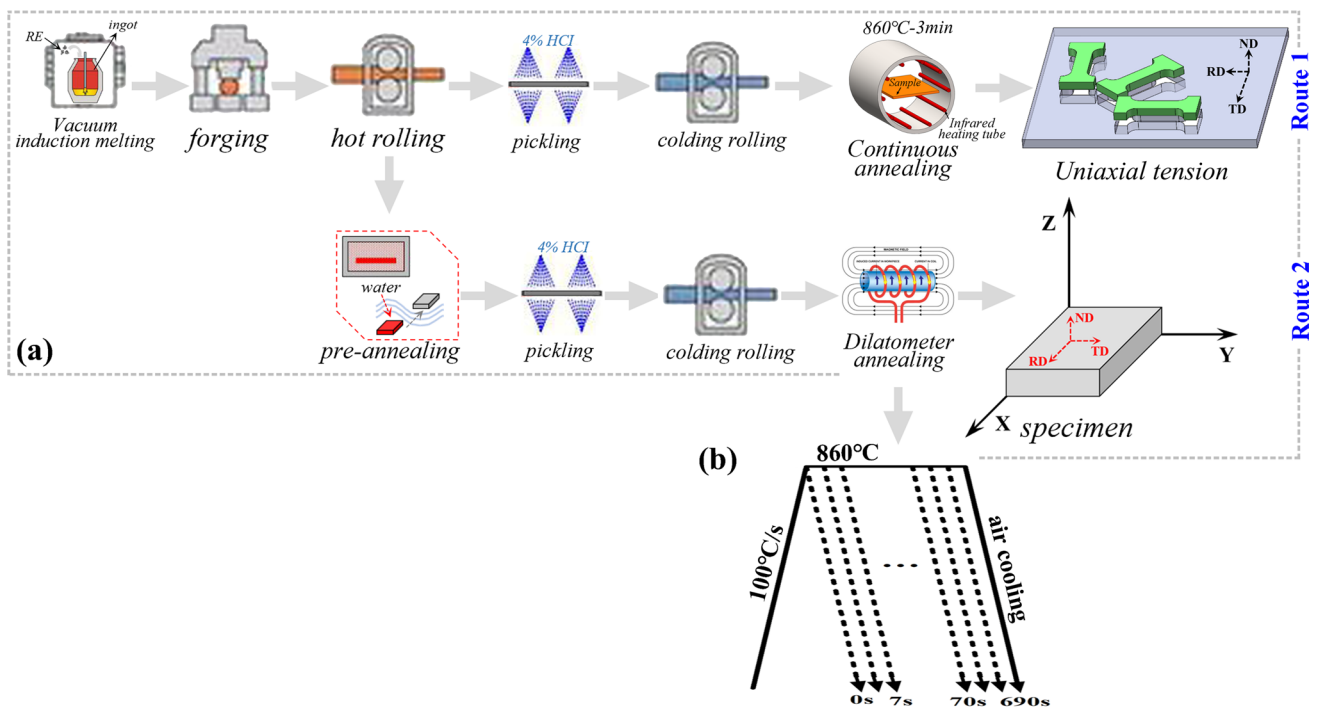


Fig. 1 a Complete production process for IF steels in two distinct routes, b heat treatment schedule for simulated annealing in dilatometer

Table 1 Chemical composition of the investigated IF steels (in wt%)

Steel grades	C	Si	Mn	S	Ti	Nb	RE	Fe
Normal-IF steel	0.0028	0.02	0.10	0.0021	0.062	0.046	–	Bal.
RE-IF steel	0.0025	0.02	0.09	0.0009	0.063	0.046	0.0025	Bal.

was introduced to eliminate the influence of early dynamic recrystallization. As illustrated in Route 2, these strips were pre-annealed at 900 °C of different times for IF steels and then quenched into water. The in-depth consideration of this pre-annealing step was to achieve similar microstructures and textures between these two types of samples before cold-rolling. After that, these pre-annealed strips would suffer pickling and be further cold-rolled in exactly the same way as that in Route 1. At the final step of simulated annealing, specimens with a dimension of 6 mm × 10 mm × 1 mm were rapidly heated to 860 °C at a constant rate of 100 °C/s and kept for different times in a thermal dilatometer then followed by the forced-air cooling to ambient temperature for the sake of instantaneous recrystallization. In this study, these schedules of different holding times assisted by forced-air cooling would be collectively referred as “interrupted annealing”.

Planar dog-bone-shaped specimens with a gauge length of 50 ± 0.1 mm and width of 25 ± 0.1 mm were sampled from the annealed plates in directions of 0°, 45° and 90° deviated from the rolling direction (see Route 1), respectively. At least 3 pieces of each direction were stretched to obtain the arithmetical average of plastic strain ratios

($r_{15\%}$) and then substituted into the following formula [24] to calculate its weighted average \bar{r} :

$$\bar{r} = \frac{r_0 + 2r_{45} + r_{90}}{4}$$

The microstructure and texture were characterized by a field emission scanning electron microscope (FE-SEM, ZEISS MERLIN Compact) equipped with electron back-scattered diffractometer (EBSD, Symmetry). The EBSD scans were performed on the cross-section (normal direction-rolling direction plane) and mid-thickness section (rolling direction–transverse direction plane, see Route 2). In the reconstructed EBSD maps, grain boundaries have been illustrated according to the misorientation angle: low-angle grain boundaries (LAGBs, 2°–15°), middle–high-angle gain boundaries (M-HAGBs, 15°–50°) and ultra-high-angle grain boundaries (U-HAGBs, > 50°), arranging in an increasing gradient of mobility driven by the lifted interfacial energies as well as misorientation angles behind this study [25]. Moreover, grain detection was guaranteed with critical misorientation of 2° and distinguishable pixels of 10 within each grain at least. After this reconstruction,

the microstructure in EBSD maps could be further divided into three different groups: (i) “deformed part” if the average misorientation angle within one grain exceeds the user-defined minimum subgrain angle of 2° , (ii) “substructure part” if some grains consist of subgrains whose internal misorientation is under 2° , but the misorientation from subgrain to subgrain is bigger than 2° , and (iii) “recrystallized part” accounts for the remaining grains in which no subgrains exist and the inside misorientation no more than 2° . Meanwhile, the orientation distribution functions (ODFs) were calculated using the harmonic series expansion method with a series rank of 22 and a Gaussian half-width of 5° ; then, $\varphi_2 = 45^\circ$ sections of Euler space were intercepted to illustrate typical orientation fibres or textures, in which the volume fraction of these textures were calculated with the tolerance of 15° . Furthermore, transmission electron microscopy (TEM, FEI Talos F200X) was used to investigate the substructure morphology of thin foil samples prepared using electrolytic double spraying (-25°C , 40 V) with 10% perchloric acid alcohol solution.

3 Results

In Route 1, the weighted average (\bar{r}) of plastic strain ratio in RE-IF steels has been improved to 2.23 from 1.93 of Normal-IF steels, increased by 16%. This mainly attributes to the lifted texture ratio of $\{111\}\langle uvw \rangle$ to $\{001\}\langle 110 \rangle$, as collected in Table 2. However, an unexpected phenomenon of grain coarsening also occurred in RE-IF steels, which seems to deviate from the consensus of RE elements assisting in grain refinement [21]. It is necessary to clarify the relation of lifted texture ratio and grain coarsening as well as influences of RE therein; this is exactly the main idea of this study: confusion of hot-rolled structure heredity had been excluded ahead of time; then, the effect of RE elements on microstructure and texture evolution of IF steels was to be strictly studied based on Route 2.

3.1 Microstructure Evolution

The pre-annealed microstructures and corresponding pole figures of both IF steels are shown in Fig. 2. It is clear that the chosen pre-annealing conditions prepared these two different

Table 2 Statistics of \bar{r} values, texture ratio and grain sizes of IF steels subjected to Route 1

Aspects	Normal-IF steels	RE-IF steels
Weighted average, \bar{r}	1.93	2.23
Texture ratio	27	41
Annealed grain sizes	13.65 μm	16.50 μm
Hot-rolled grain sizes	7.43 μm	10.36 μm

kinds of samples with a very similar grain size and texture distribution, which sets an important initial condition for investigating the recrystallization behaviour between these two kinds of IF steels during the following processing steps. After simulated annealing, the microstructure evolution of interrupted annealed IF steels is shown in Fig. 3, divided into nucleation stage (0–20 s), grain growth and coarsening stage (20–690 s) according to the holding time. At initial stage of nucleation with 0 s holding time (see Fig. 3a₂, b₂), the microstructure still retained the elongated morphology inherited from cold-rolled states (see Fig. 3a₁, b₁). Owing to the inhomogeneous strain distribution among deformation bands (DBs), only a few grains nucleated from prior grain boundaries, and the remaining regions still largely maintained banded states with higher dislocation density. With an increase of holding time to 3 s, more and more recrystallized grains appeared as marked by white arrows (see Fig. 3a₃, b₃), sometimes even intragranular nucleation took place. Until this stage, no obvious difference was found between the Normal-IF steel and RE-IF steel, but as the holding time further increased to 10 s, nucleation process in the Normal-IF steel almost completed (see Fig. 3a₄), while traces of fragmented deformed substructures with $\{001\}\langle uvw \rangle$ orientation still existed in the RE-IF steel owing to incomplete recrystallization (see Fig. 3b₄). With longer holding time (see Fig. 3a_{5–9}, b_{5–9}), the annealed microstructure evolved into the grain growth and coarsening stage, and started to show significant differences between these two kinds of steels. The residual structural fragments in the RE-IF steel were engulfed by recrystallized grains, and more $\{hkl\}\langle 111 \rangle$ grains started to appear, while grains with $\{001\}\langle uvw \rangle$ orientations faded out gradually. Although those new born grains in the Normal-IF steel might exhibit slightly bigger grain size at the nucleation stage, grain coarsening of the RE-IF steel rapidly happened, and it eventually obtained much bigger grains than that of the Normal-IF steel.

After grouping limited by the misorientation, the microstructure in EBSD maps had been divided into three different groups, consisting of deformed part, substructure part and recrystallized part, respectively. The area percentages of these three parts at the nucleation stage (up to 20 s holding time) are summarized in Fig. 4a, showing the proportion of deformed grains reduced significantly and then taken over by the recrystallized grains with increasing holding time. However, no clear trend was found in the “substructure” part, suggesting the subgrains exist through the whole nucleation stage. The average grain size of the top five largest grains for different holding times at the nucleation stage is further summarized in Fig. 4b. It is clear that the maximum grain size and recrystallization area in the RE-IF steel are consistently smaller than the Normal-IF steel; this refinement effect that was directly related to the sluggish reshaping behaviour of DBs preserved for the whole nucleation stage. Therefore, it is believed that grain boundary migration and

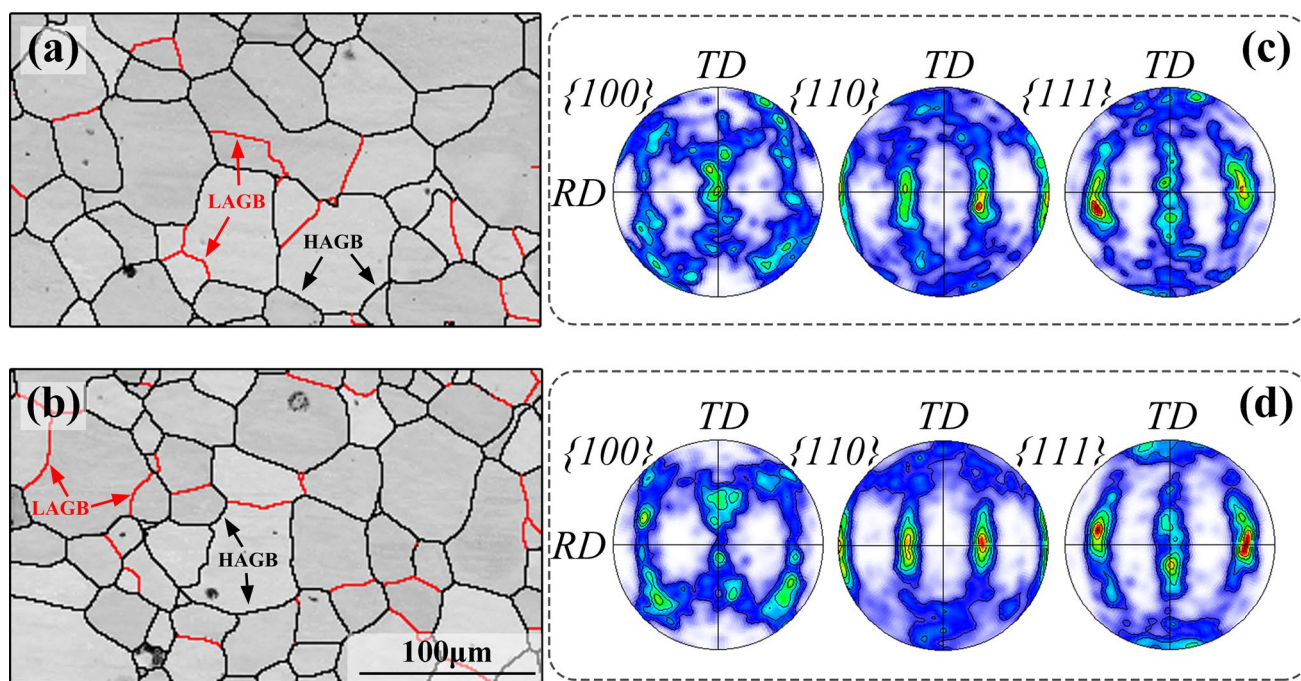


Fig. 2 Pre-annealed microstructures of **a** the Normal-IF and **b** the RE-IF steel, **c, d** correspond to pole figures of these two microstructures, respectively

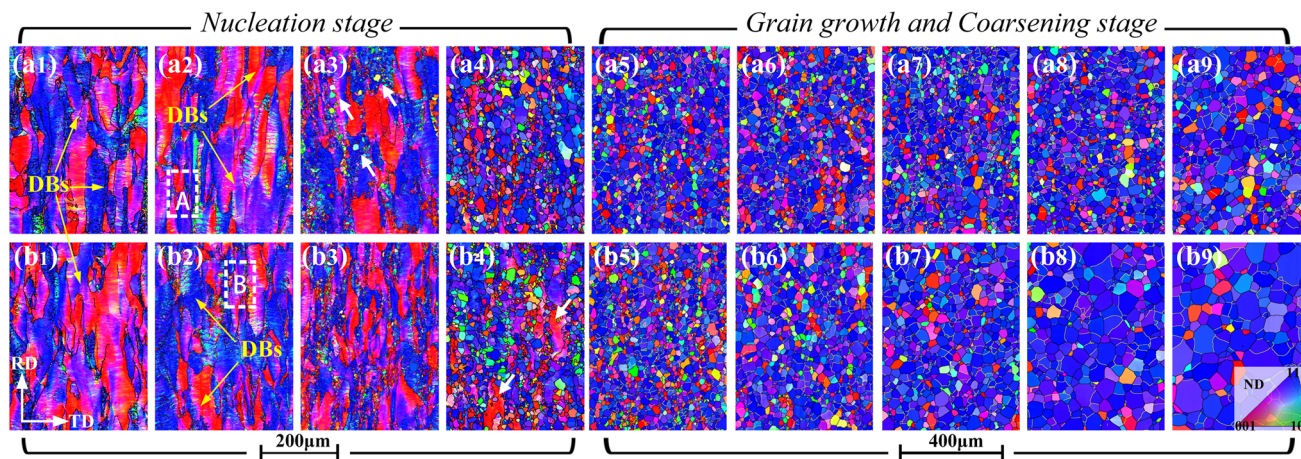


Fig. 3 Microstructures of **a** the Normal-IF steel and **b** the RE-IF steel samples from **a**₁, **b**₁ cold-rolled states to various interrupted annealed states of different holding times: **a**₂, **b**₂ 0 s; **a**₃, **b**₃ 3 s; **a**₄, **b**₄ 10 s; **a**₅, **b**₅ 50 s; **a**₆, **b**₆ 80 s; **a**₇, **b**₇ 90 s; **a**₈, **b**₈ 210 s and **a**₉, **b**₉ 690 s, wherein the microstructure evolution is divided into two major stages separated by the critical holding time of around 20 s encountering the recrystallization fraction of more than 96%

even the dislocation rearrangement of the RE-IF steel were significantly hindered, coming across the consensus of grain refinement with RE addition [21, 26]. This is also consistent with the observation in Fig. 3b₄, where the RE-IF steel shows sluggish nucleation behaviour within residual $\{001\}\langle uvw \rangle$ distorted grains. However, the grain sizes show very different trends during grain growth and coarsening stage. Statistic in Fig. 4c reveals that the average grain size of the RE-IF steel

was getting close to that of the Normal-IF when the holding time increased from 20 to 60 s, then abnormally became bigger at around 65 s, and eventually became twice bigger than the grain size of the Normal-IF steel when finishing the interrupted annealing. The rapid grain growth in the RE-IF steel is believed to be related to the preferential growth of the new born grains with special orientations [9], which will be further elaborated in the following discussion sections.

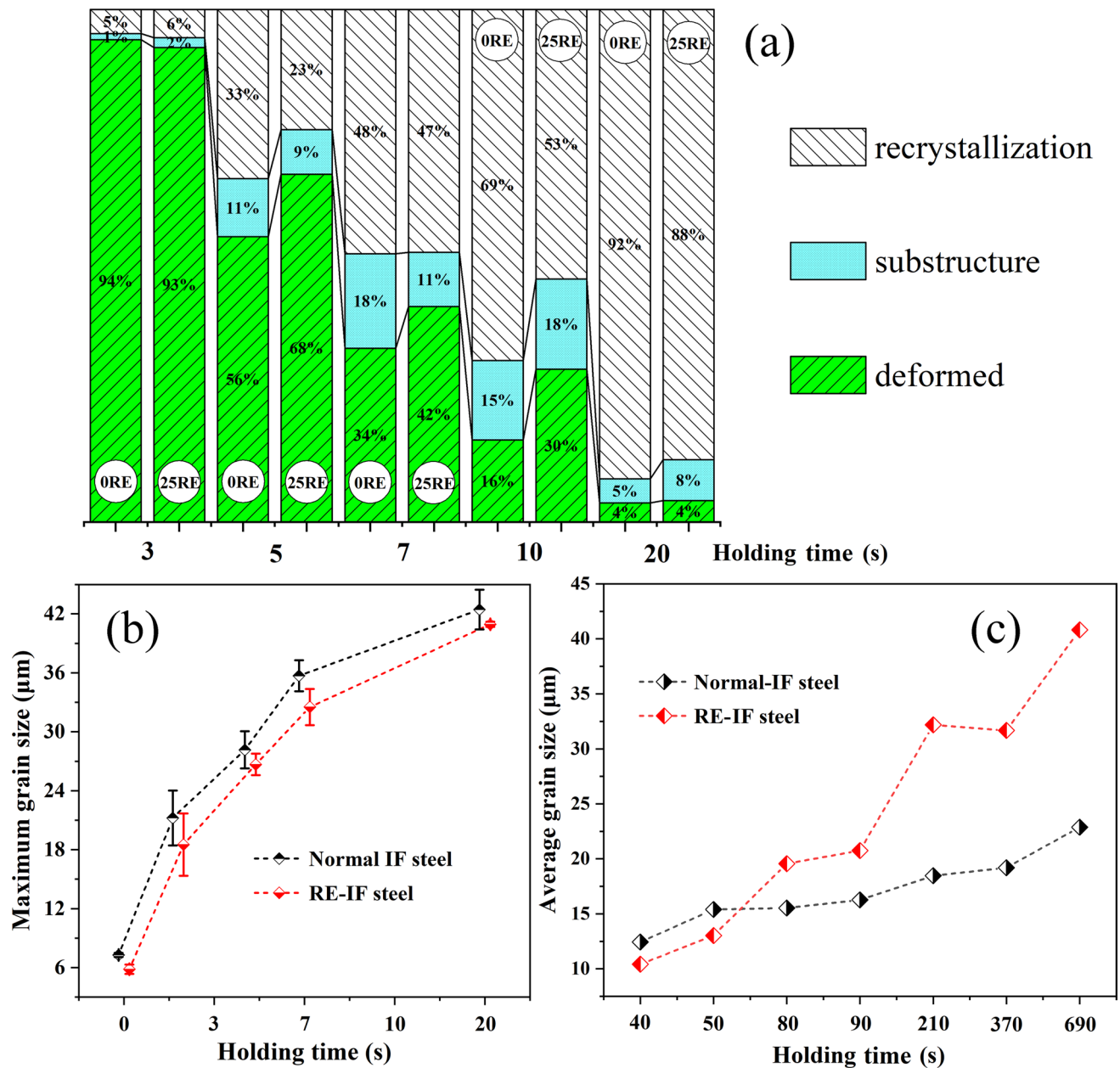


Fig. 4 Statistics of microstructural fraction and grain size of the investigated steels during static recrystallization: **a** area percentage of microstructure groups at the nucleation stage, **b** average grain size of top five largest grains at the nucleation stage, **c** average grain size of fully recrystallized IF steel samples during grain growth and coarsening stage

3.2 Texture Transformation

For body-centred cubic (BCC) crystals, the α -fibre textures mainly consisting of $\{001\}\langle 110\rangle$, $\{112\}\langle 110\rangle$ and $\{111\}\langle 110\rangle$ components are normally associated with plastic deformation as their $\langle 110\rangle$ axes parallel to rolling direction, while γ -fibre textures primarily consisting of $\{111\}\langle 110\rangle$, $\{111\}\langle 112\rangle$ and $\{554\}\langle 225\rangle$ components are often found after recrystallization [3, 8, 9]. These γ textures are capable of resisting thickness thinning due to

relatively higher elastic modulus along the $\langle 111\rangle$ direction hence less common after plastic deformation [27]. Because there is only 5° difference between the $\{111\}\langle 112\rangle$ and $\{554\}\langle 225\rangle$ orientations [9], they are both referred as $\{554\}\langle 225\rangle$ orientation in the following discussion unless otherwise specified. To investigate the role of RE elements in the texture configurations of IF steels, the ODFs of cold-rolled and annealed samples were obtained and reconstructed as shown in Fig. 5a–d. Although the Normal-IF and the RE-IF steel after cold-rolling both showed deformed

configurations with strong α -fibre and weak γ -fibre, the intensity of $\{001\}\langle 110\rangle$ and $\{112\}\langle 110\rangle$ components were indeed enhanced in the RE-IF steel, in good agreement with previous observations reported by Wang et al. [24]. After CA, α -fibre textures associated with plastic deformation almost disappeared, while the γ -fibre textures became the only dominating textures, confirming that the samples were fully recrystallized. Moreover, the maximum intensity of γ -fibre in the RE-IF steel is about 1.5 times higher than the Normal-IF steel, largely due to the textures inherited from the cold-rolling state.

For the purpose of clarifying texture transformation details, the orientation distribution function $f(g)$ and volume fraction Δg at different holding times were also calculated and are plotted in Fig. 6. In analogy with aforementioned microstructure evolution, the texture transformation process was also divided into two major stages: nucleation stage, and growth and coarsening stage. At the initial nucleation stage, more $\{112\}\langle 110\rangle$ and $\{001\}\langle 110\rangle$ components of α -fibre textures were observed in the RE-IF steel compared with the Normal-IF steel. As these two components both have $\langle 110\rangle$ orientation direction but a rotation angle of 35° , they would often

be found adjacent after cold-rolling (see more discussions in chapter 4.3). It was also reported that this $35^\circ\langle 110\rangle$ misorientation exhibited higher boundary mobility [28], to offer the favourable growth direction towards distorted structures [29, 30], which is believed to account for the significant reductions of both volume fraction and ODFs for $\{112\}\langle 110\rangle$ and $\{001\}\langle 110\rangle$ textures during nucleation stage in this study. The fraction profile line of $\{001\}\langle 110\rangle$ texture also shows slow reduction at the beginning of the nucleation stage when holding time is less than 3 s, attributed to the alternation of distinct nucleation rates. Compared to these α -fibre textures, relatively low percentage of γ textures were found in both Normal-IF and RE-IF steels at the nucleation stage then started to increase as the holding time increased. It is interesting to point out that the profile lines of γ textures in the Normal-IF steel showed a drop at early holding time, as highlighted by dotted boxes and connected by a dash line in Fig. 6a, confirming the sequential nucleation of γ -fibre textures [5]. Both the $\{554\}\langle 225\rangle$ and $\{111\}\langle 112\rangle$ components of γ -fibre textures increased continuously and exhibited cumulative content advantage until coarsening stage, but the $\{111\}\langle 110\rangle$ component reached a peak content at around 60–70 s of holding

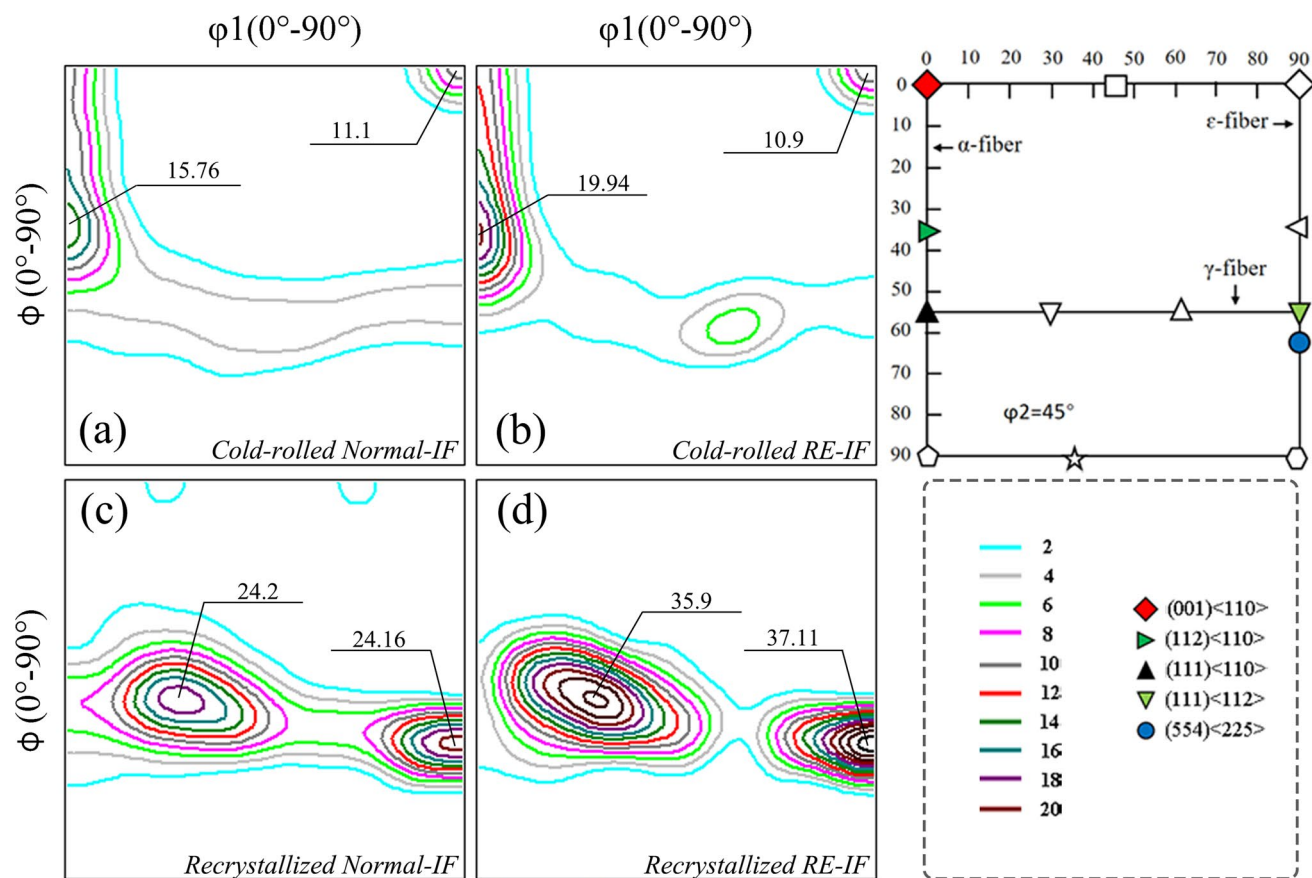


Fig. 5 $\varphi_2=45^\circ$ ODF sections of **a** the cold-rolled Normal-IF steel, **b** the cold-rolled RE-IF steel, **c** the fully recrystallized Normal-IF steel, **d** the fully recrystallized RE-IF steel and their corresponding standard $\varphi_2=45^\circ$ section with typical orientation fibres and textures of cubic system

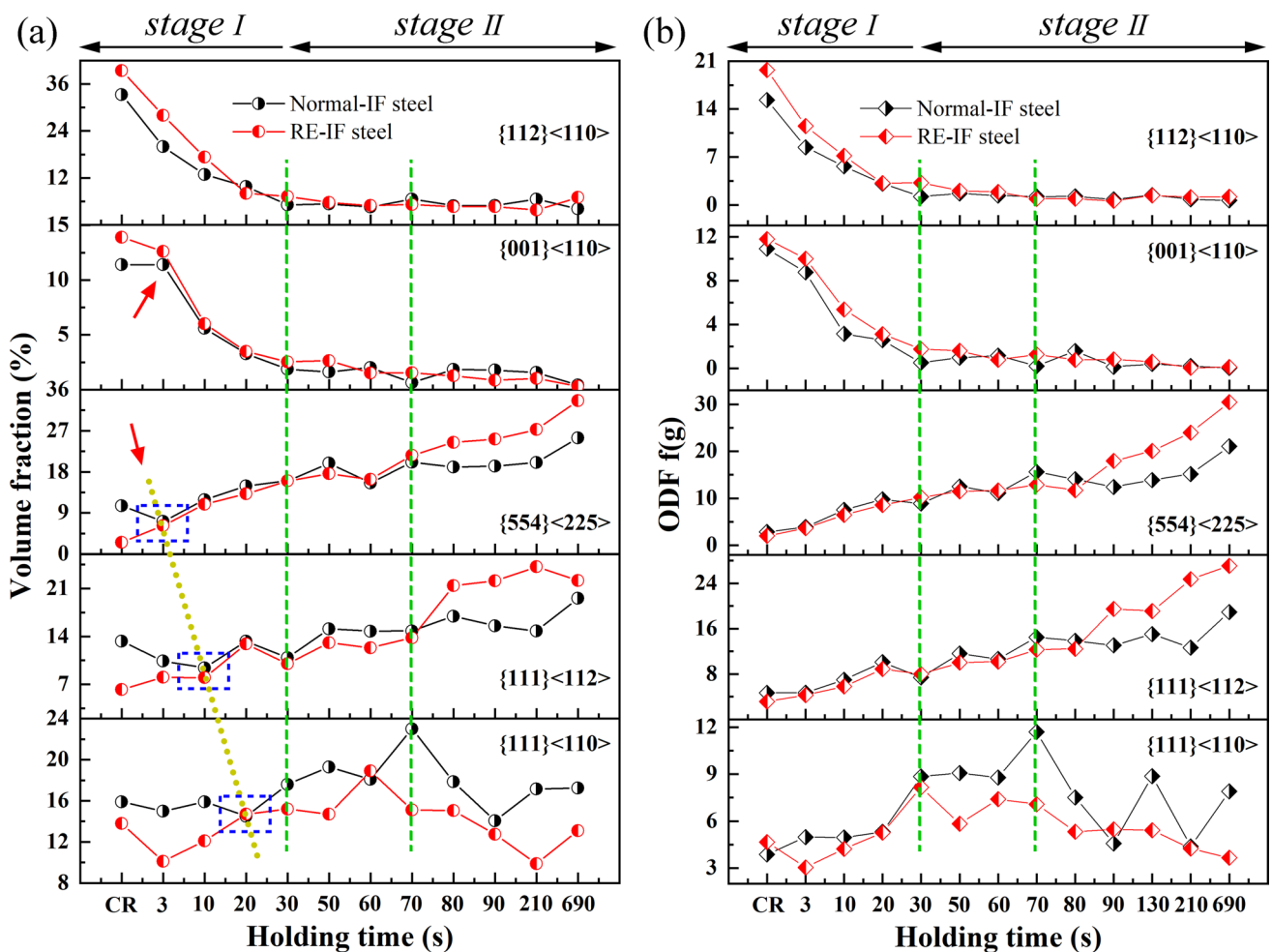


Fig. 6 **a** Volume fraction Δg , **b** orientation distribution density $f(g)$ of typical textures in the Normal-IF steel and the RE-IF steel, in which the volume fraction is calculated with the tolerance of 15°

time before decreasing to almost the initial level. On account of these observations during annealing, it is clear that the α textures associated with deformation continued to reduce and became almost disappeared after the annealing, instead, γ -fibre textures associated with recrystallization increased except $\{111\}\langle 110\rangle$, contributing to main process of texture transformation. In particular, the RE-IF steel had a much stronger orientation advantage of $\{554\}\langle 225\rangle$ and $\{111\}\langle 112\rangle$ textures and maintained these textures through grain coarsening stage. Considering these distinct transformation behaviours within γ -fibre, there might be other evolution paths to accelerate the formation of $\{554\}\langle 225\rangle$ and $\{111\}\langle 112\rangle$ orientations, rather than the fluctuations of volume fraction or ODF intensity throughout annealing process, like the expression of $\{111\}\langle 110\rangle$ texture.

3.3 Dislocation Distribution

During the nucleation stage, new grains primarily appeared from the existing microstructures with high degree of disorder (such as prior grain boundaries and shear bands) and then started to grow up with the cost of the residual grain fragments inherited from the previous cold-rolling process. The principal consideration of the driving force for this process is focused on “stored energy” [31], often associated with lattice distortion and defects introduced by plastic deformation. It is believed that this kind of stored energy is mainly caused by dislocation behaviours, as other types of lattice defects usually make minor contributions [32]. These dislocations are further classified into geometrically necessary dislocations (GNDs) and statistically stored dislocations (SSDs), depending on whether it can accommodate lattice curvature (related to homogeneous or non-homogeneous deformation) [31, 33]. In view of the triaxial compressive stress states of cold-rolled sheet and its intrinsic anisotropy,

it is believed that non-homogeneous strain was accounted for the compatible deformation of IF steels in this study, proved by the uneven distribution of DBs illustrated in Fig. 3a₁, b₁. Oliferuk et al. [34] also reported that almost all metal and alloys, with the exception of single crystal or at uniform deformation, are plastically non-homogeneous to some extent on account of their plastic strain gradients. Therefore, one could assume that the contribution from SSDs to the stored energy could be neglected, and hence, the study was focused on the stored energy from GNDs and its influence on the recrystallization behaviour during the annealing process.

In view of the fact that the lattice curvatures caused by GNDs correspond to those measurable local intergranular misorientations, the GNDs density could be estimated by reprocessing the EBSD maps, as shown in Fig. 7. The

GNDs density-frequency curves obtained from the two different types of IF steel samples at the cold-rolled state are plotted in Fig. 7a, where a peak could be clearly identified at relatively high dislocation density region; it is also found that the whole RE-IF steel curve shifted to left as compared with the Normal-IF steel curve (see the local enlargement Fig. 7a₁), that is, the occurrence probability of high energy regions (HERs) R1 increased while that of ultra-HERs R2 decreased, indicating a higher dislocation density state in the Normal-IF steel after cold-rolling. At the beginning of annealing with 0 s holding time, the original broad peaks at the relatively high dislocation density region shifted slightly towards the left, while remaining a similar GND density gap between the two curves (see Fig. 7b). The shifting was obviously caused by the atom rearrangement during annealing,

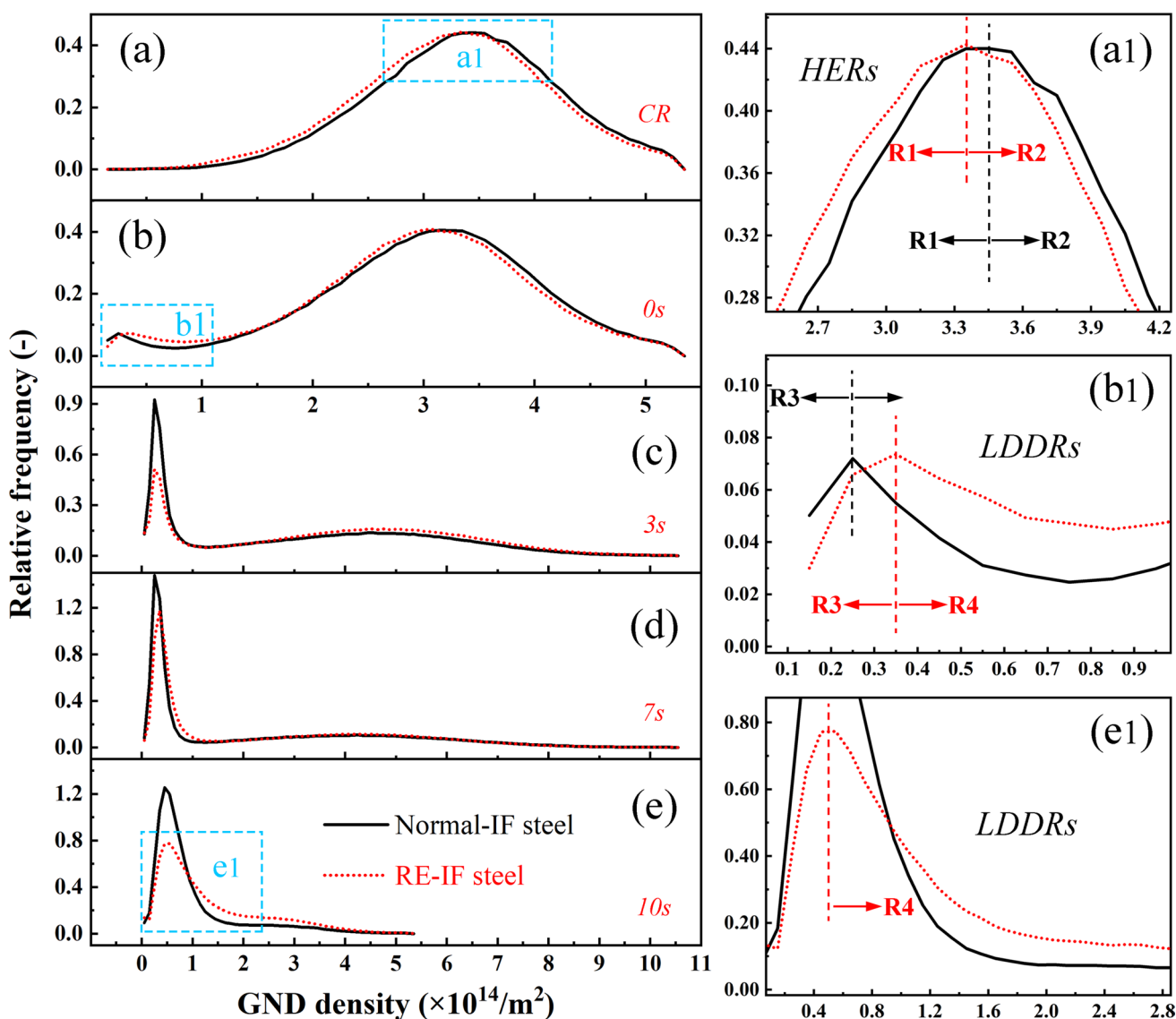


Fig. 7 GNDs density of experimental steels at a cold-rolled state and annealed states with different holding times: b 0 s, c 3 s, d 7 s and e 10 s, wherein the local enlarged drawings a1, b1 and e1 correspond to selected areas in a, b and e, respectively

and the gap indicates that the Normal-IF steel still maintained a higher dislocation density state at this stage. It is also worth pointing out that new peaks started to appear at low dislocation density regions (LDDRs) for both the Normal-IF steel and the RE-IF steel, corresponding to the preferential nucleation at the prior grain boundaries observed in Fig. 3a₂, b₂. More details in the local enlargement in Fig. 7b₁ showed that the RE-IF steel curve is shifted more towards right, indicating more incomplete recrystallized LDDRs R4, originated from the solute-drag effect introduced by RE elements directly or indirectly. It is believed that whether the recrystallized nuclei form from mismatch areas or the new born grains invade surrounding substructures, the deformed microstructure evolves from substructure to recrystallized structure through the formation of subgrain boundaries (SGBs) or LAGBs originated from dislocation rearrangement and the migration of LAGBs towards HAGBs [35]. After thermal activation, the nucleation of distorted structure occurred rapidly, accelerating the massive transformation from ultra-high or HERs to ultra-low or LDDRs accompanied with sharp decrease of dislocation density. The faster nucleation rate of the Normal-IF steel made the stored energy quickly release and brought about more ultra-low or LDDRs in 3-s holding time (see Fig. 7c). As the holding time further increased, the magnitude of the original peaks reduced significantly and almost disappeared within 10 s holding time, while the magnitude of the new sharp peaks increased a lot (see Fig. 7c–e). The new peaks corresponding to the new born grains indicated that these new grains indeed had low dislocation density. Actually, there were still traces of residual fragmented substructures in the RE-IF steel, suggested by the sharper curve of the Normal-IF steel than the RE-IF steel curve at LDDRs especially for 10-s holding time (see the local enlargement Fig. 7e₁), because the added RE elements could hinder the dislocation rearrangement during nucleation stage directly or indirectly [6, 21] and then delay the recrystallization process.

4 Discussion

4.1 Activation of Slip Systems and Resultant Deformation Textures

Since slip system represents the possible spatial orientation of slipping deformation [35], it is widely accepted that the formation of a certain crystallographic orientation is the collective result of various slip systems [36]. For α -ferrite, there exist three different kinds of slip systems including $\{110\}_6\langle 111 \rangle_2$, $\{112\}_{12}\langle 111 \rangle_1$ and $\{123\}_{24}\langle 111 \rangle_1$. It was reported that $\{110\}_6\langle 111 \rangle_2$ and $\{112\}_{12}\langle 111 \rangle_1$ slip systems could operate together to undertake the majority of plastic deformation for ultra-low carbon steels with BCC structure [37], but it is not clear how these slip systems would contribute to the

orientation evolution. Our study of IF steels would shine some light on this issue. Although similar initial microstructures were strictly guaranteed between the Normal-IF and the RE-IF steel, much more deformation textures were found aggregating to α -fibre in the RE-IF steel, so it is believed that RE elements could affect the action sequence of the three slip systems and change the texture configurations after plastic deformation. However, the whole activation process of any particular slip system and its interaction with other slip systems through the deformation process could not be directly observed by experiments. In view of the different feedbacks of various slip systems towards external strain or stress, the visco-plastic self-consistent (VPSC) model [38] was introduced to integrally predict the reorientation, shape change of individual grains and the resultant texture transformation associated with plastic deforming. The simulated ODFs calculated using the VPSC model for the Normal-IF and the RE-IF steel after plastic deformation are shown in Fig. 8a, b. The details, including the smooth transition of γ -fibre in Normal-IF steel and the orientation segregation of α -fibre in the RE-IF steel, were carefully captured, agreeing well with the experimental ODFs (see Fig. 8c, d) restructured from the EBSD maps as shown in Fig. 3a₀, b₀, which suggests that the adopted model parameters including crystallographic files, boundary conditions as well as thresholds selection are very suitable for the simulation of slip system activation and orientation evolution in IF steels.

In Fig. 9a, b, the relative activities of the three slip systems in IF steels are calculated as a function of equivalent plastic strain according to the verified VPSC model, and the corresponding slip plane relationships are schematically described as well. It is shown that $\{112\}_{12}\langle 111 \rangle_1$ slip system of ferrites in the Normal-IF steel is active to support the initial plastic deformation at 0–0.1 low strain level (see Fig. 9a), compelling a large number of $\{112\}$ slip planes nearly parallel to the rolling plane so that the $\{112\}\langle uvw \rangle$ orientations could be massively formed. Meanwhile, $\{110\}$ slip planes of partial ferrites have been rotated to the positions with about 20° to rolling surface due to the 19.47° intersection angle between $\{110\}$ and $\{112\}$ crystal planes, as shown in Fig. 9b. With increase of plastic strain, $\{110\}_6\langle 111 \rangle_2$ slip system starts to reach its critical resolved shear stress (CRSS) then becomes active as well, while the movement of previously activated $\{112\}_{12}\langle 111 \rangle_1$ slip system is restrained during the strain range of 0.1–0.8. This proportion shift of “as one falls, another rises” between the $\{112\}_{12}\langle 111 \rangle_1$ and $\{110\}_6\langle 111 \rangle_2$ slip systems made the $\{110\}_6\langle 111 \rangle_2$ component become the dominant slip system during steady-state strain of more than 0.8, which would compel part of $\{112\}\langle uvw \rangle$ ferrites continues rotating to other positions whose $\{110\}$ slip planes almost have 35° angle with rolling surface. In view of the 35.26° intersection angle between $\{110\}$ and $\{111\}$ crystal planes [28], partial $\{112\}\langle uvw \rangle$ orientations would turn into $\{111\}\langle uvw \rangle$

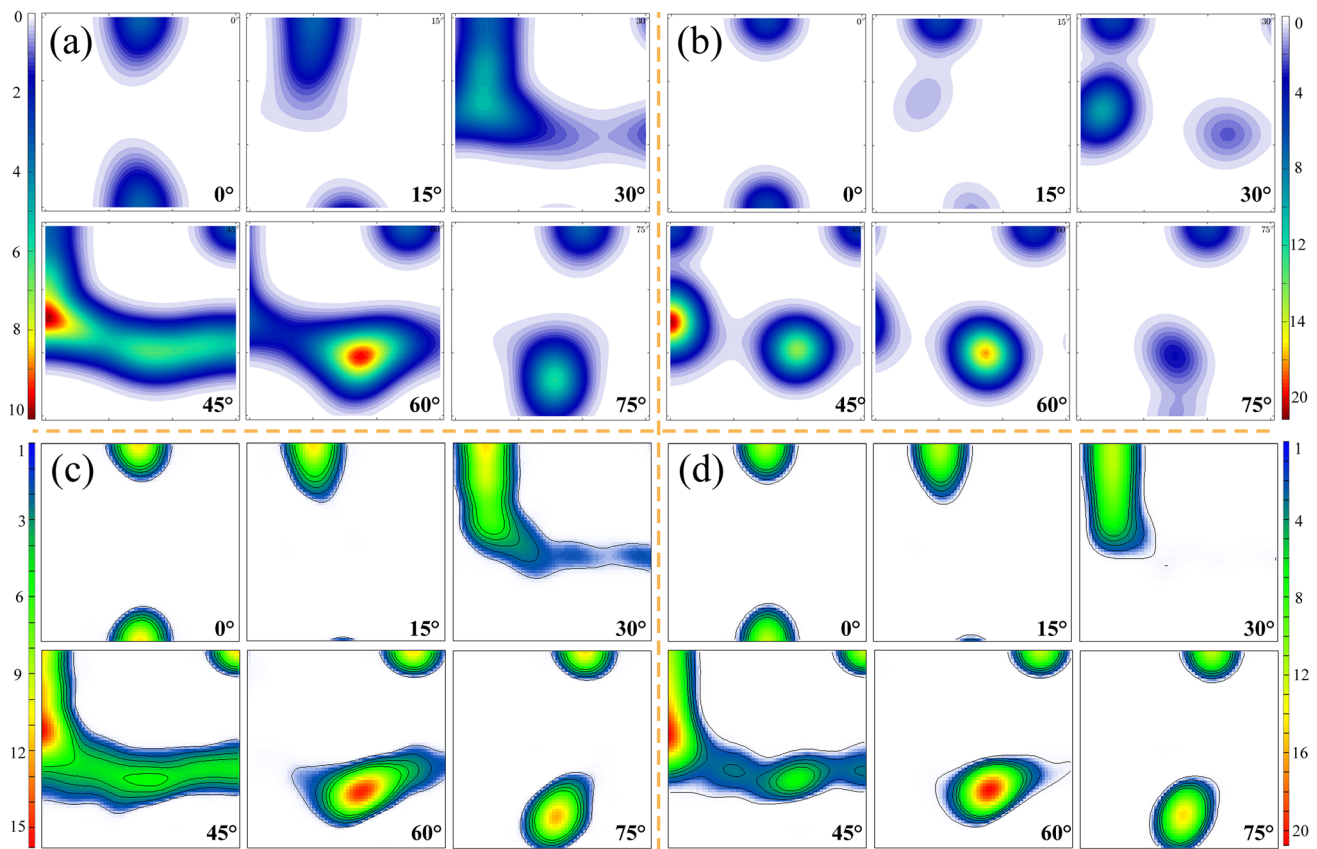


Fig. 8 **a, b** Simulated ODFs calculated by the VPSC model, **c, d** experimental ODFs reconstructed from the EBSD maps of **a, c** Normal-IF steel and **b, d** RE-IF steel

orientations after severe plastic deformation, accounting for the deformation texture configuration with strong α -fibre and weak γ -fibre components in the Normal-IF steel.

For the RE-IF steel, $\{110\}_6\langle 111\rangle_2$ and $\{112\}_{12}\langle 111\rangle_1$ slip systems easily reach their CRSS at initial strain and start to slide almost simultaneously, followed by avalanche multiplication of $\{112\}_{12}\langle 111\rangle_1$ and sharp reduction of $\{110\}_6\langle 111\rangle_2$ when reaching the 0.1 plastic strain (see Fig. 9a). After this rapid evolution, a large number of grains with $\{112\}\langle uvw\rangle$ orientations appeared in the existing microstructure where abundant $\{112\}$ slip planes nearly parallel to the rolling plane, suggesting the majority of $\{110\}$ slip planes in these $\{112\}\langle uvw\rangle$ grains stayed in states with about 20° to rolling surface, while few grains continued to rotate to the plane with around 35° to rolling surface. As the reduction further increases, the steady state of $\{112\}_{12}\langle 111\rangle_1$ slip system in the RE-IF steel is reached and stabilized until the end of cold-rolling deformation, leading to the distinct α -fibre-rich texture in the RE-IF steel.

In view of the different slip systems start-up-sequence in IF steels during rolling deformation, it was found that the movement of $\{110\}_6\langle 111\rangle_2$ slip system was inhibited in the RE-IF steel as compared with the Normal-IF steel, in which

the inhibiting effect of RE elements on $\{110\}_6\langle 111\rangle_2$ slip system could be further analysed from the perspective of interstices density on $\{110\}$ slip plane. Since the difficulty of dissolved RE characterizing in experiment, thermodynamic calculation of phase diagram (by Thermal-Calc, see Fig. 9c) was accepted to deduce the existence forms of RE elements in IF steels. In process of solidification, sulphur elements firstly reacted with RE elements and RE-oxysulfides formed [19–21], then the remaining sulphur would be captured by titanium elements to form $Ti_2S_2C_4$ or metastable TiS precipitations [6]; thus, it should have been more titanium elements converting from compound states (i.e., $Ti_2S_2C_4$ and TiS) into solution states. Moreover, the added RE elements were mainly used to modify the detrimental inclusions, while the remaining part would dissolve in ferrite matrix [21]. The work hardening capacity provided by $\{110\}_6\langle 111\rangle_2$ slip systems, and their stress response to equal strain, greatly changed in IF steels as disturbed by dissolved Ti and RE atoms, leading to the significant alternation of stress continuity and the relative-activity refit of the three kinds of slip systems during rolling deformation. After strain accumulation, the activation of one or more certain slip systems would become stable and support the different

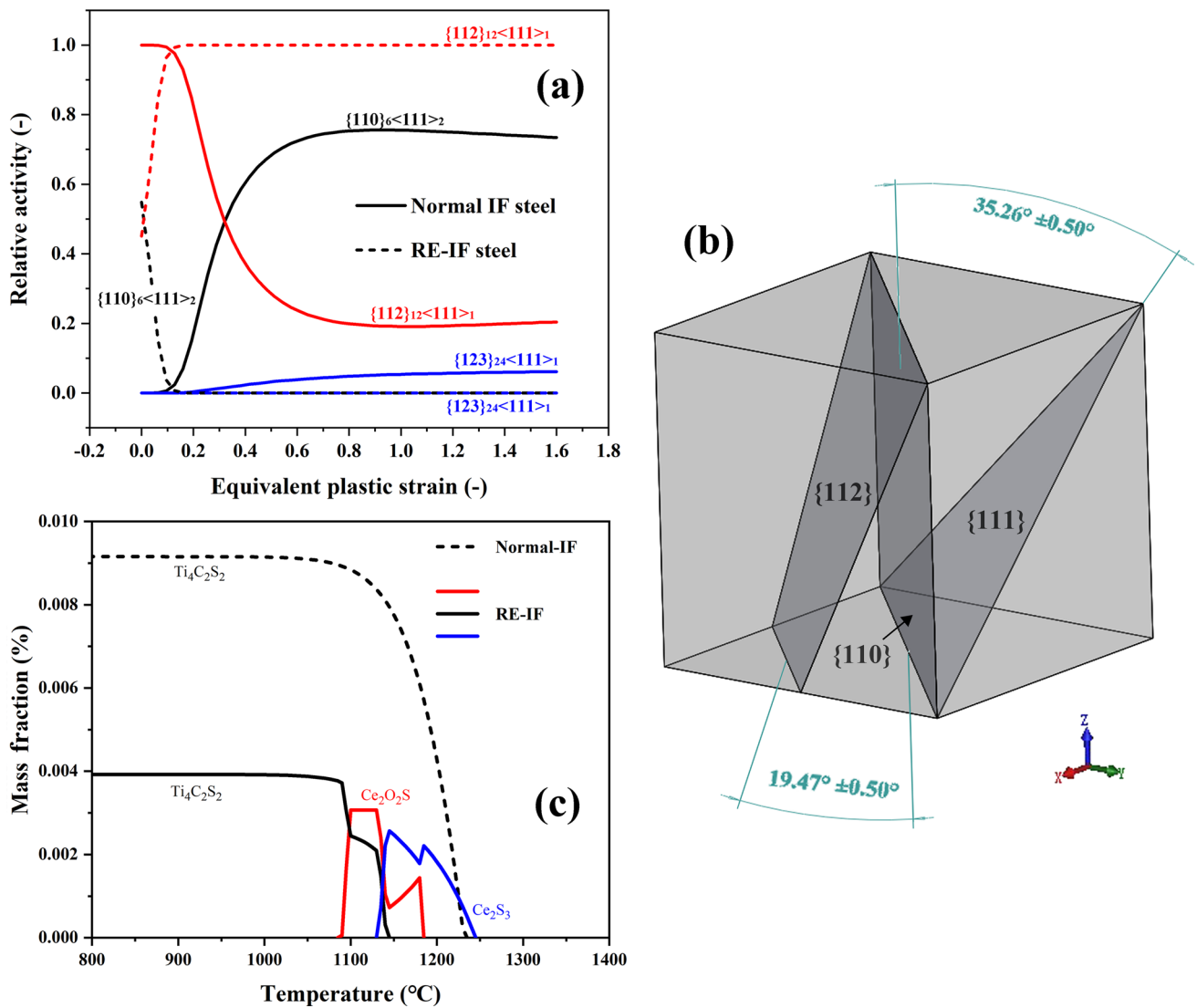


Fig. 9 Calculated **a** relative activities of $\{110\}_6\langle 111\rangle_2$, $\{112\}_{12}\langle 111\rangle_1$ and $\{123\}_{24}\langle 111\rangle_1$ slip systems in IF steels undergoing rolling deformation, and the **b** schematic diagram of orientation relationships among $\{112\}$, $\{110\}$ and $\{111\}$ slip planes, as well as **c** thermodynamic calculation of interaction behaviour among steelmaking elements for IF steels before and after RE addition

texture configurations within IF steels during severe plastic deformation.

4.2 GNDs Distribution within Deformation Textures and Associated Nucleation Sequence

During plastic deformation, the dislocation movement in $\{110\}_6\langle 111\rangle_2$ slip system was inhibited in the RE-IF steel, where much more $\{110\}$ slip planes kept in states with around 20° to rolling surface and no long rotated, resulting in massive formation of deformation α -fibre components especially the $\{112\}\langle uvw\rangle$ textures. However, there was not enough stored energy accumulated and allocated in RE-modified matrix (see Fig. 7a), the nucleation rates of deformation textures in the RE-IF steel would vary with

that of the Normal-IF steel. With increasing holding time, typical textures in IF steel samples were distinguished and GNDs densities within these defined textures are collected in Fig. 10. It is confirmed that the deformation textures in the Normal-IF steel would always have higher stored energy (see Fig. 10a) regardless of their volume fractions, while the stored energy sequence of deformation textures in both IF steels remained unchanged and still arranged in the decreasing magnitude of $E_{\{554\}\langle 225\rangle} \approx E_{\{111\}\langle 112\rangle} > E_{\{111\}\langle 110\rangle} > E_{\{112\}\langle 110\rangle} > E_{\{001\}\langle 110\rangle}$, in accordance with oriented nucleation sequence proposed by Nagataki and Hosoya [5]. Based on this, slight microstructure evolution assisted with dislocation rearrangement initially occurred in severely distorted areas mostly occupied by $\{554\}\langle 225\rangle/\{111\}\langle 112\rangle$ textures. After that, the stored energy in $\{554\}\langle 225\rangle$ type

textures was rapidly released and the solid-line curve of the RE-IF steel significantly shifted to left compared to the Normal-IF steel (see Fig. 10b), guaranteeing the faster recovery rate and continuously increasing volume fraction of $\{554\}\langle 225\rangle/\{111\}\langle 112\rangle$ textures in the RE-IF steel as described in Fig. 6a. However, the minimum volume fraction of initial deformation $\{554\}\langle 225\rangle$ type textures limited its contribution to the overall recrystallization rate, and there were not much more ultra LDDRs R3 existing in the RE-IF steel for recrystallized $\{554\}\langle 225\rangle$ type textures, which suggested the incomplete recrystallization of deformed $\{554\}\langle 225\rangle$ type textures maybe resulted from the lower exhausted energy because the majority of stored energy had been used for their nucleation behaviours. Unlike the former new born $\{554\}\langle 225\rangle$ type textures, the recrystallized

subgrains with $\{111\}\langle 110\rangle$ orientation started to appear as well and their nucleation rates in the Normal-IF steel were faster than that of the RE-IF steel, it is not only due to the higher stored energy within deformed $\{111\}\langle 110\rangle$ texture (see Fig. 10b), but also the higher volume fraction in the Normal IF steel shown in Fig. 6a. Although the GNDs existing in the deformation γ -fibre textures were sensitive to thermal activation, only slight recrystallized grains preferentially nucleated from the prior grain boundaries [7], agreeing very well with the minor recrystallization morphology of DBs illustrated in Fig. 3a₂, b₂. Before that, there were no significant differences of $\{112\}\langle 110\rangle$ textures in both IF steel samples except the shrinking magnitude gap of their approaching stored energy curves. With increasing holding time to 3 s (see Fig. 10c), the relative occurrence

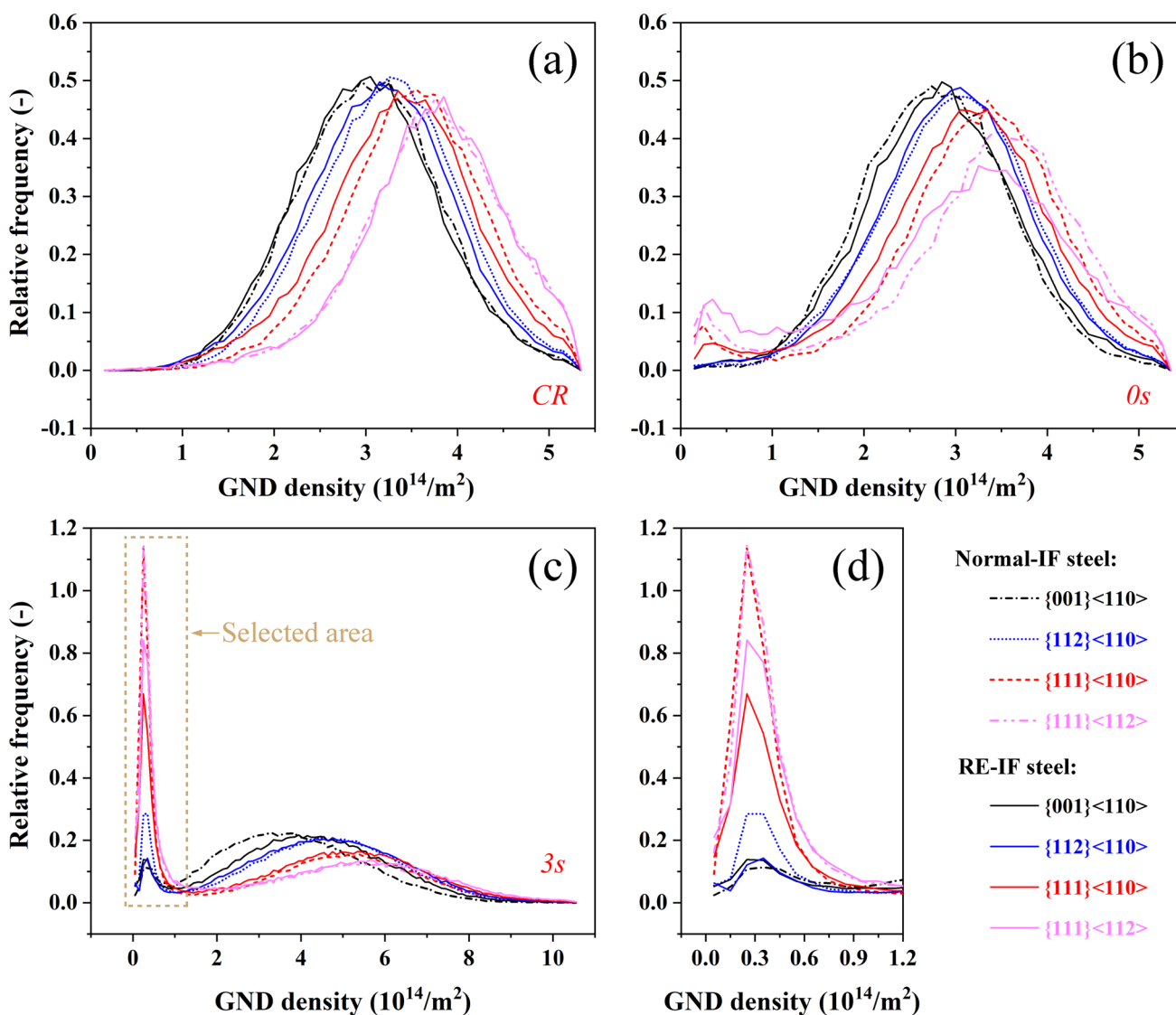


Fig. 10 GNDs statistics within typical textures of investigated IF steels from a cold-rolled states to annealed states with holding times of b 0 s and c 3 s, respectively, in which the selected area marked with dashed rectangle is locally enlarged in picture d

frequency of recrystallized $\{112\}\langle 110\rangle$ texture in the Normal-IF steel was about two times higher than that of the RE-IF steel even though there were much more deformation α -fibre textures existing in the RE-IF steel, which suggested the nucleation rate instead of the initial volume fraction became the controlling factor of texture transformation for $\{112\}\langle 110\rangle$ component. As for $\{001\}\langle 110\rangle$ component, it is found that the stored energy curve of the Normal-IF steel significantly shifted to left during heating process, another obvious energy gap between the two IF steel samples reappeared at isothermal stage (Fig. 10b, c) and the deformed $\{001\}\langle 110\rangle$ texture in the Normal-IF steel had lower stored energy different from that at the initial state as shown in Fig. 10a. However, there were few recrystallized grains with $\{001\}\langle 110\rangle$ orientation existing in both annealed Fe-matrices especially the Normal-IF steel, as shown in local enlargement Fig. 10d, maybe caused by the slowest nucleation rate and competitive disadvantage among all of the deformation textures.

It is believed that dislocation rearrangement and further microstructure degeneration easily occur at the positions where higher deformation energy stored [3, 7], so that the nucleation rates of major deformation textures in the Normal-IF steel were faster than that in the RE-IF steel except $\{554\}\langle 225\rangle$ type textures controlled by volume fraction, ensuring much complete recrystallization behaviour of the Normal-IF steel as shown in Fig. 3a. For RE-IF steels, excess Ti elements in solid solution would increase the activation energy for recrystallization kinetics [39, 40], and dissolved RE elements also tended to segregate at crystal defects, e.g. grain boundaries and vacancies [21]. Therefore, it is not easy for grain boundaries, especially the SGBs and LAGBs consisted of dislocations [41], to escape from the solute-drag effect of dissolved Ti or RE elements. The microstructure evolution from distorted states to annealed states was significantly inhibited in the RE-IF steel, revealing the sluggish nucleation behaviour and finer grain size within RE-modified Fe matrix during the nucleation stage.

4.3 Texture Transformation and Corresponding Microstructure Evolution

In Sect. 4.2, it is found that even minor differences of stored energy partition within deformation textures could make significant influence on grain nucleation rates, although RE elements added into IF steels had little effects on the nucleation sequence of deformation textures. To clarify the nucleation sites and associated sequential nucleation behaviour of different deformation textures within distorted Fe matrix, the selected areas A and B in Fig. 3a₂, b₂ are magnified in Fig. 11a, b and further examined against the oriented nucleation theory. It is clear that the deformation γ -fibre textures evidenced by $\{111\}$ pole figures $A_{i=1-4}$ also had priority to

recover [8] and were transformed into chain-like substructures (shear bands undergoing annealing somewhat) whose inclination angles are around 35° – 90° against rolling direction within ferrites, corresponding to the intragranular shear bands with 25° – 35° inclination angles along rolling direction within RD-ND plane [28, 42], as shown in Fig. 11c. To distinguish this new born chain-like substructure from its precursor, shear bands in the cold-rolled Normal-IF sheet were further characterized by TEM and are displayed in Fig. 11d. The TEM micrograph shows that the deformation shear bands separated with subgrain boundaries were composed of a series of approximately parallel microbands with spacing of around 200–400 nm, in which the selected area electron diffractions (SAED) pattern of area F crossing two microbands did not split, indicating that crystallographic orientations of microbands were closed to each other and the misorientations among them were extremely small or even negligible. On account of this, the misorientations along the yellow arrow crossing areas marked in Fig. 11a, b are reprocessed in Fig. 12a, b by EBSD method, respectively. It is found that most of the misorientations among these microbands were less than 3° from point-to-point analysis in both the Normal-IF steel and the RE-IF steel, while a few misorientations greater than 3° but less than 5° occasionally occurred only in the Normal-IF steel. After accumulation of numerous tiny misorientations, obvious intragranular misorientation more than 25° and intense local strain would arise in shear bands easily found in prior coarse grains, so that dislocation rearrangement preferentially took place within these extremely distorted areas [3, 8], promoting the formation of rod-like subgrains around microbands until original shear bands were completely replaced. On account of the higher misorientation accumulation, as demonstrated in Fig. 11c, several recrystallized $\{554\}\langle 225\rangle$ type grains even arose with the sacrifice of shear bands or rod-like subgrains in the Normal-IF steel, agreeing well with previous results reported that intragranular shear bands were considered as the preferred nucleation sites for recrystallized γ -fibre textures [1–3]. However, there were other regions with lower stored energies, e.g. $\{001\}\langle 110\rangle$ and $\{112\}\langle 110\rangle$ textures verified by pole figures $B_{i=1,2,3}$ and $C_{i=1,2,3}$, respectively, still maintaining the elongated morphology till the end of nucleation. Since the fact that stored energy in the RE-IF steel was less than that of the Normal-IF steel, it is clear that there were more residual grain fragments with $\{001\}\langle uvw\rangle$ orientations in the Normal-IF steel as shown in Fig. 3b₄, b₅, which once again confirmed the conclusion that deformation $\{001\}\langle 110\rangle$ orientation remained stable during the whole nucleation stage [7]. Unlike the former, the $\{112\}\langle 110\rangle$ orientation with two variants of $C_{i=1,3}$ and $C_{i=2}$ usually located at the sides of deformation γ -fibre components along the rolling direction. There were few recrystallized nuclei but recovered subgrains existing in ribbon $\{112\}\langle 110\rangle$ structures related to the incomplete

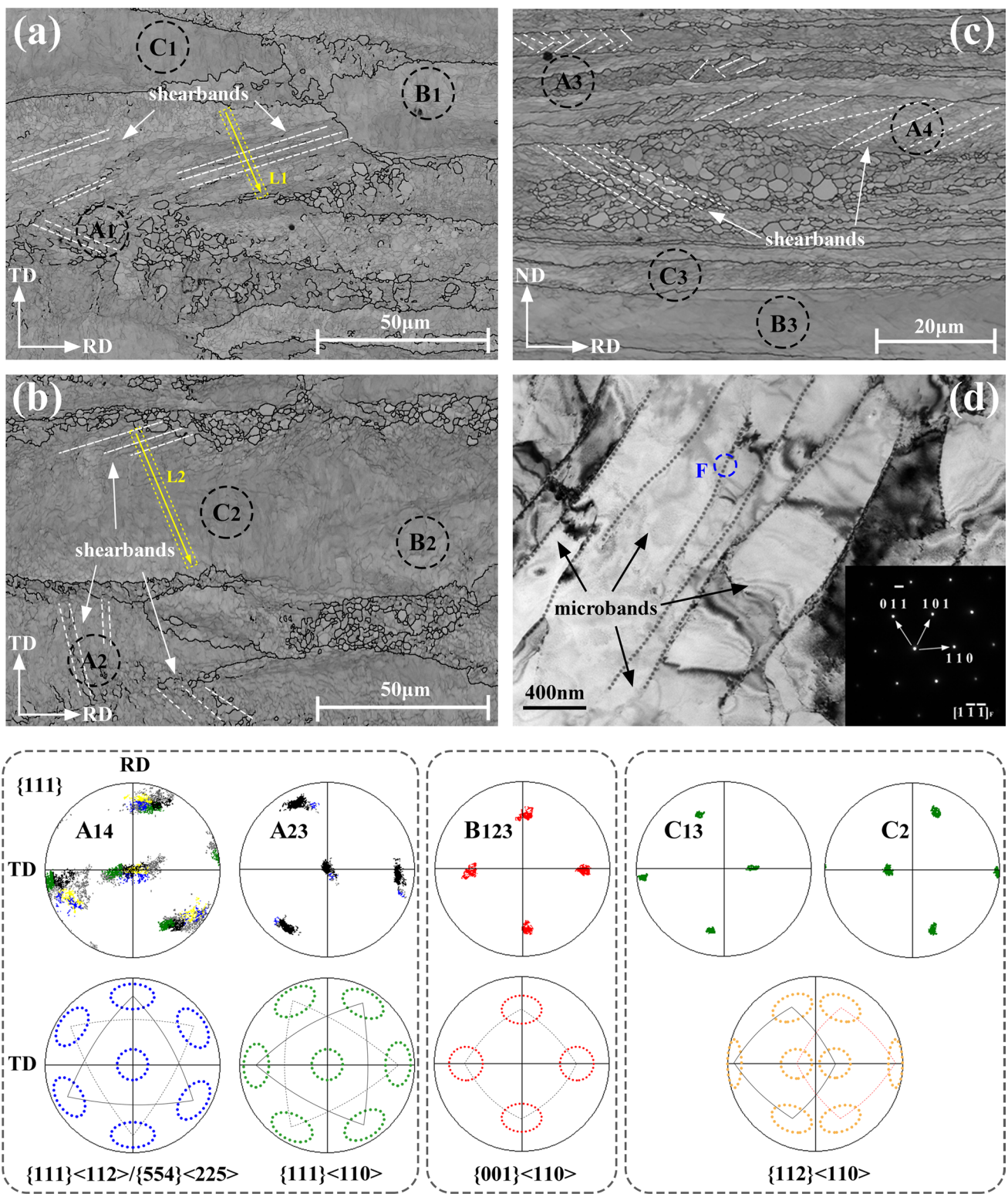


Fig. 11 Local enlargements of selected areas A-B from Fig. 3a₂, b₂ and oriented nucleation behaviours of **a** the Normal-IF steel and **b** the RE-IF steel, **c** simultaneous nucleation morphology of the Normal-IF steel but in RD-TD plane. These special regions marked as A_{*i*=1,2,3,4}, B_{*i*=1,2,3}, and C_{*i*=1,2,3} were traced to typical crystallographic orientations of {111}<*uvw*>/<554><225>, {001}<110> and {112}<110> respectively, in which the rod-like subgrains in A_{*i*=4} originated from shear bands composed of several microbands illustrated in **d**

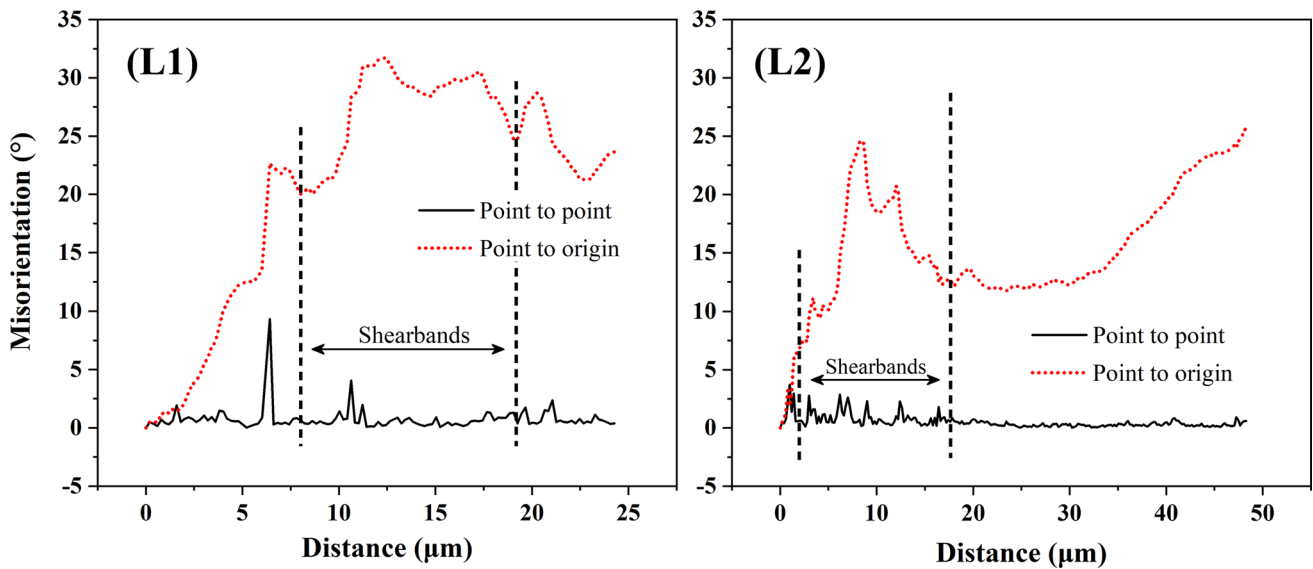


Fig. 12 Misorientation variation of the shear bands within γ -fibre textures: (L1) shear bands in RD-TD plane of the Normal-IF steel; (L2) shear bands in RD-TD plane of the RE-IF steel, where the selected shear bands were marked by yellow arrows in Fig. 11a, b

recrystallization, this sluggish recovery behaviour was usually observed in the RE-IF steel because it had the maximum $\{112\}\langle 110\rangle$ fraction compared to the Normal-IF steel. In view of the distinct texture configuration and stored energy sequence, the aforementioned sequential nucleation behaviours of three different kinds of deformation textures were well corresponded to the Johnson–Mehl–Avrami–Kolmogorov (JMAK) model [7] with segmented recrystallization kinetics, in which the deformation γ -fibre textures usually existed much more intragranular shear bands had priority to nucleate, while the α -fibre textures recovered slowly and then delayed the whole nucleation stage, resulting in sluggish recrystallization process of the RE-IF steel compared to the Normal-IF steel.

Apart from nucleating from shear bands, there were also other favourable paths for grains with γ -fibre orientations to recrystallize from the deformed matrix, and all these nucleation paths are shown in Fig. 13. After 7-s holding time, the nucleation process of fully recovered rod-like subgrains (mostly existing in deformed γ -fibre textures) was completed and their banded morphology (shown in selected area D of Fig. 13a) almost disappeared within seconds. Besides, the nucleation of $\{554\}\langle 225\rangle$ type grains also easily took place at prior grain boundaries such as the positions E_1 and E_2 where $\{112\}\langle 110\rangle$ orientation neighbours on $\{001\}\langle 110\rangle$ orientation, this coincided with the results [43] that the prior grain boundaries accumulated higher stored energy compared with other grain boundaries, were considered to be favourable nucleation sites for recrystallized grains with γ -fibre orientations [44, 45]. After nucleation, these new born γ -fibre grains would

sweep up the non-recrystallized regions on both sides and even formed the recrystallized chain-like zones, as marked by the enclosed dash-rectangle area E_2 within RD-ND plane. In addition to the nucleation from shear bands and grain boundaries, it is also found that the grains with γ -fibre orientations could simultaneously or separately recrystallize from the deformation α -fibre regions through oriented nucleation [5, 45]; thus, three areas $F_{i=1,2}$ and G were selected from Fig. 13a, b to clarify the details of oriented nucleation in this study. In selected area F_1 , recrystallized grain with $\{554\}\langle 225\rangle$ type orientations was observed to nucleate from the deformation $\{112\}\langle 110\rangle$ texture regions individually, and it also could recrystallize from the undesirable $\{001\}\langle 110\rangle$ texture regions alone, as shown in F_2 . Besides, combined formation of recrystallized γ -fibre orientation grains took place frequently in IF steels because these undesirable regions could provide numerous nucleation sites for $\{554\}\langle 225\rangle$ and $\{111\}\langle 112\rangle$ orientation grains simultaneously, like the selected area G. Once the subgrains converted into recrystallized grains, they would constantly engulf the surrounding deformed Fe-matrix until these newborn grains contacted with each other [9]. Since there were much more deformation α -fibre textures, as well as lower stored energy partition, existing in the RE-IF steel, part of elongated structure with $\{001\}\langle uvw\rangle$ orientations still existed in Fe-matrix after 7 s heat preservation at 860 °C, while connected ribbon structures in the Normal-IF steel almost had been broken up due to the complete recrystallization.

With increasing holding time, the residual structure fragments in both steel samples were completely replaced

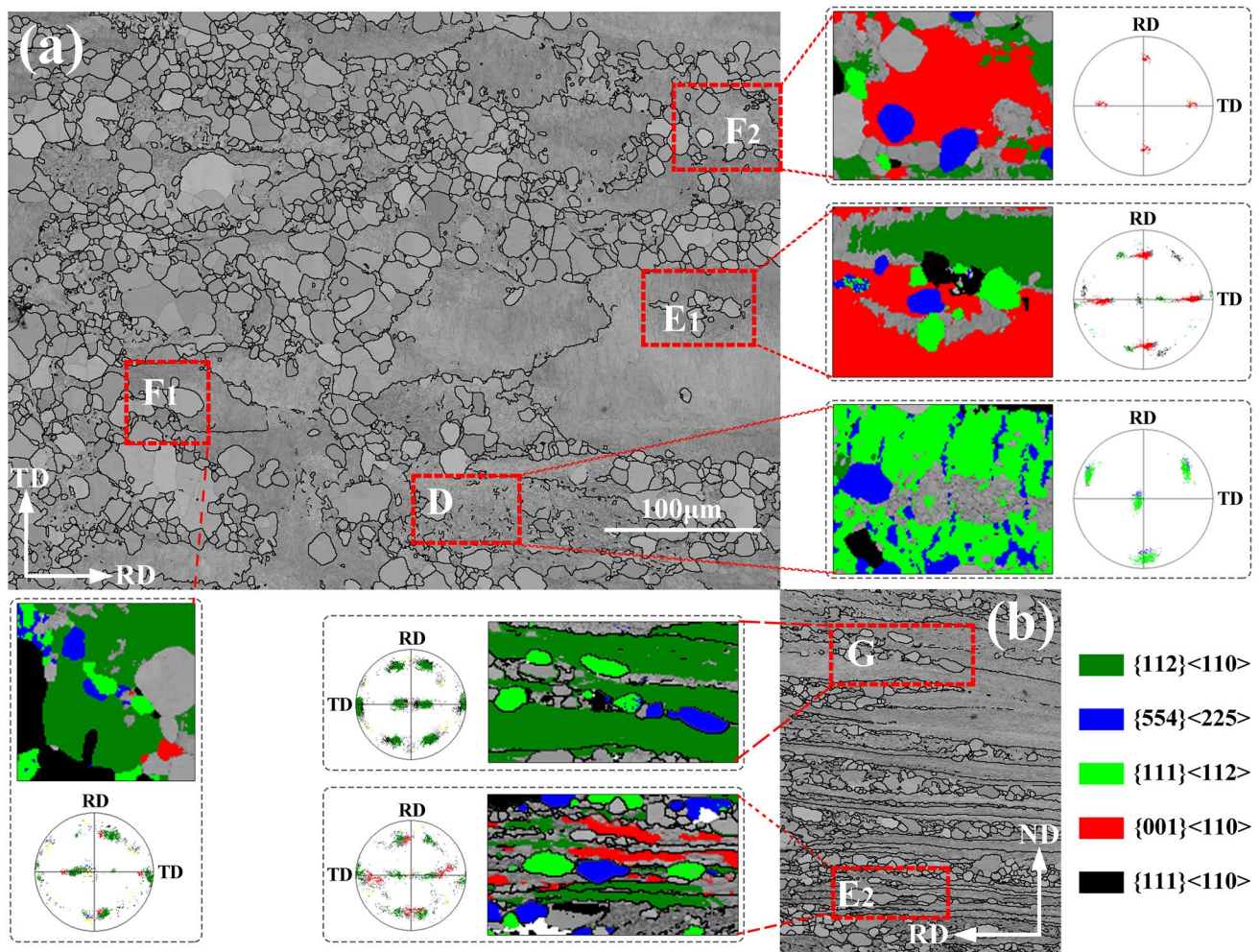


Fig. 13 Different nucleation paths of γ -fibre orientation grains from deformed Fe-matrix: **a** RD-TD midplane, **b** RD-ND plane of the Normal-IF steel with 7 s holding time

by equiaxed strain-free grains, in which these new born grains except for several α -fibre grains were mainly used to generate the γ -fibre orientations of various proportions. As described in Fig. 6a, the volume fractions of the $\{554\}\langle 225\rangle$ and $\{111\}\langle 112\rangle$ textures in the RE-IF steel were similar to that of the Normal-IF steel at the end of nucleation (around 30 s holding time), but the RE-IF steel still had the nucleus advantage on accounts of its finer grains and potential nucleation sites, e.g. shear bands, prior grain boundaries and cold-rolled α -fibre textures. For the Normal-IF steel, however, a relatively larger amount of deformation γ -fibre textures were observed to provide more nucleation sites for the recrystallized grains preferentially, while other paths nucleated from α -fibre or prior grain boundaries therein would become inactive according to the sequential nucleation that the deformation γ -fibre textures nucleate preferentially followed by sluggish nucleation of α -fibre textures. Furthermore, it is already found that the $\{554\}\langle 225\rangle$

type orientations whose nucleation rates were controlled by volume fraction failing to make significant contribution to the nucleation rate of initial recrystallization process, so that those new born γ -fibre grains in the Normal-IF steel were mainly dominated by $\{111\}\langle 110\rangle$ orientations with both grain size and volume fraction advantages after nucleation, as already shown in Figs. 4a and 6a. In view of the existed differences among the three nucleation paths in both IF steel samples, the competitive growth of these new born grains with γ -fibre orientations would account for the grain coarsening phenomenon in the RE-IF steel.

Since the fact that only coarse grains larger than the average grain size have positive contribution to the grain coarsening phenomenon, the volume fractions of γ -fibre textures within these coarse grains are collected in Fig. 14a, b to separate the later stage of normal grain growth from abnormal grain coarsening. It is clear that the texture fractions of the Normal-IF steel varied in small amplitude while that

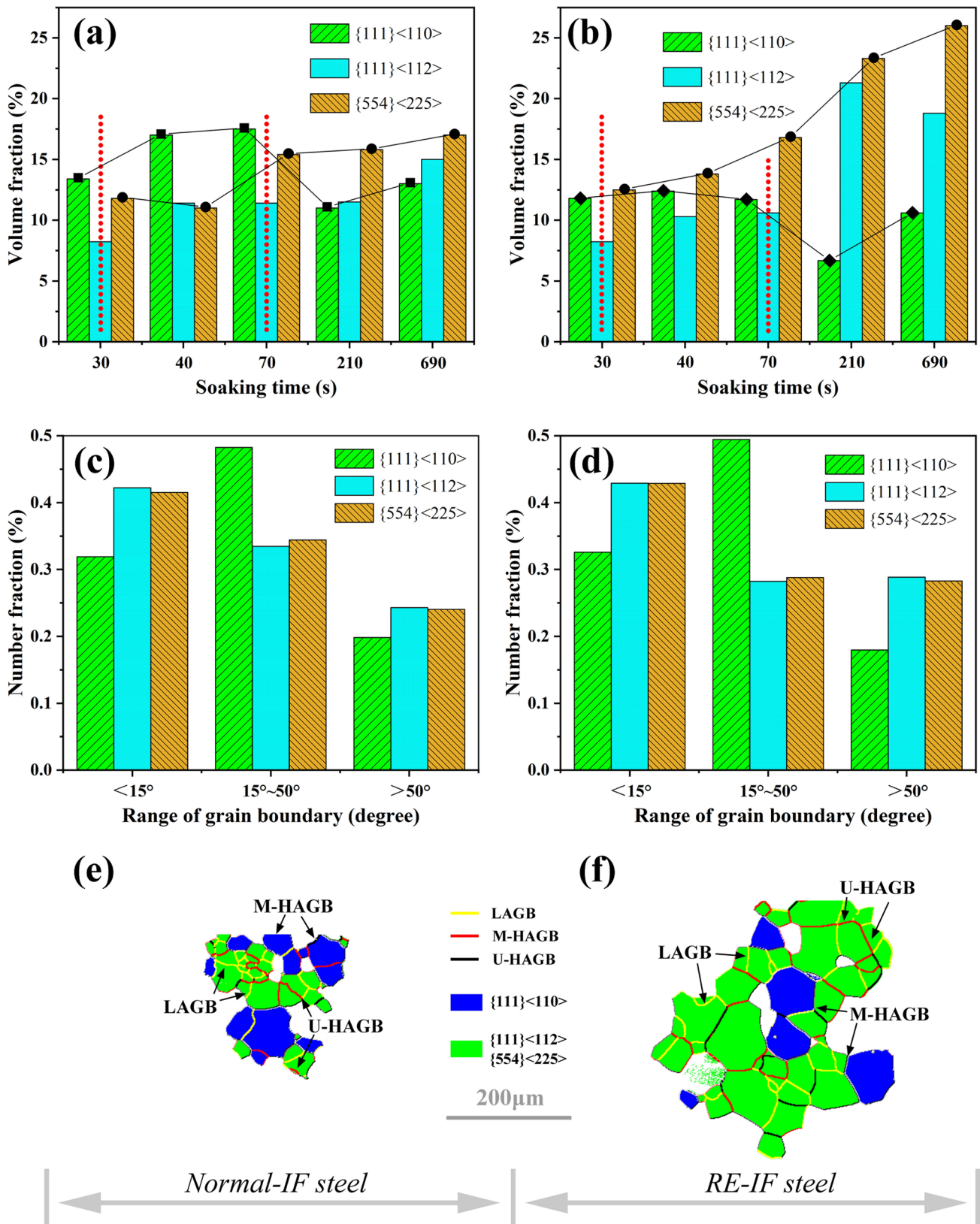


Fig. 14 **a, b** Volume fraction of γ -fiber orientations within coarse grains, **c, d** number fraction of grain boundaries within γ -fiber grains, **e, f** morphology of orientation clusters in **a, c, e** the Normal-IF steel and **b, d, f** the RE-IF steel

of the RE-IF steel even became twice as the initial states, suggesting that there indeed existed obvious texture competitive growth among these γ -fibre components and the selective growth dominated by $\{554\}\langle 225\rangle$ type textures would introduce completely different grain growth state in the RE-IF steel. To further determine the migration characteristics of various orientations, grain boundaries within γ -fibre textures were also distinguished and are counted in Fig. 14c, d. Almost identical fraction configurations in both IF steel samples make it clear that RE elements could hardly change the intrinsic migration modes of γ -fibre textures but the growth rate of concrete orientation, in which the grains with $\{111\}\langle 110\rangle$ orientation were mainly observed to grow up through M-HAGBs migration while the grain growth of $\{554\}\langle 225\rangle$ type orientations primarily relied on LAGBs annihilation and U-HAGBs migration. For the studied Normal-IF steel, it is already confirmed that the growth potential of $\{111\}\langle 110\rangle$ orientation grains with both grain size and volume fraction advantages was stronger than that of $\{554\}\langle 225\rangle$ type orientation grains after nucleation, while these $\{554\}\langle 225\rangle$ type orientation grains still achieved grain growth in two different ways rather than a single method. By contrary, the $\{554\}\langle 225\rangle$ orientation grains with nucleus advantage as well as $\{111\}\langle 110\rangle$ orientation grains in the RE-IF steel intensified rapidly at the same time and further reached texture fraction equilibrium at the end of nucleation (see Fig. 14b). With increasing holding time more than 70 s, the volume fractions of γ -fibre textures in the Normal-IF steel, similar to that in the RE-IF steel but occurrence time, also reached a dynamic fraction equilibrium at the later stage of grain growth and coarsening. After that, the dominant texture transformed from $\{111\}\langle 110\rangle$ orientation to $\{554\}\langle 225\rangle$ orientation, guaranteeing the alternating distribution of γ -fibre textures in the Normal-IF steel as shown in Fig. 14e. However, since the fact that there were much more LAGBs existing in the RE-IF steel, the grain growth of that part through LAGBs annihilation would be promoted. Moreover, the grain boundary migration at grain growth and coarsening stage was dominated by HAGBs (in particular U-HAGBs have the fastest mobility [25]) that could easily get rid of solution elements but sensitive to dispersed precipitates [6, 17, 18]. On account of the reduced metastable TiS and $\text{Ti}_2\text{S}_2\text{C}_4$ precipitates in the RE-IF steel, their blocking effect on grain boundary migration would become weakened. The volume fraction of $\{554\}\langle 225\rangle$ orientation grains in the RE-IF steel would definitely exceeded that of $\{111\}\langle 110\rangle$ orientation grains and kept this $\{554\}\langle 225\rangle$ orientation advantage inherited from nucleation period much more active until the end of annealing. In brief, the grains with $\{554\}\langle 225\rangle$ type orientations always dominating the preferred-growth advantage would accelerate the formation of orientation clusters (see Fig. 14f) and further induce grain coarsening phenomenon in the RE-IF steel.

To summarize, synergic evolution of microstructure-texture-stored energy would take place in IF steels to drive the static recrystallization upon CA. Since the fact that compatible deformation behaviour of IF steels was sensitive to dissolved RE elements, the VPSC model was adopted, verified and used to calculate the relative activities of major slip systems, suggesting that different cooperation of the three slip systems would account for distinct texture configurations in IF steels after plastic deformation. Then, GNDs accumulated in these deformation textures was reconstructed to clarify the stored energy sequence, as well as distinguishable nucleation rates of varied texture components. With different texture configurations and reduced stored energy, defined textures were observed to suffer oriented nucleation and selective growth, which is the key to explain the sluggish nucleation behaviour and grain coarsening phenomenon of RE-IF steels.

5 Conclusions

In this study, the synergic evolution of microstructure-texture-stored energy in IF steels has been investigated to elaborate the effects of dissolved RE elements on static recrystallization. Based on the experimental observations and verified VPSC model, the following conclusions can be drawn:

1. RE elements can significantly influence the deformation textures configuration of IF steels and then postpone recrystallization nucleation but accelerate grain coarsening after long-term annealing.
2. The relative activities of different slip systems are sensitive to RE elements, which would make the $\{110\}_6\langle 111\rangle_2$ slip systems become extremely inactive, leading to an α -fibre textures rich configuration in RE-IF steels.
3. The stored energy sequence $E_{\{554\}\langle 225\rangle} \approx E_{\{111\}\langle 112\rangle} > E_{\{111\}\langle 110\rangle} > E_{\{112\}\langle 110\rangle} > E_{\{001\}\langle 110\rangle}$ remains unchanged in RE-IF steels, but nucleation rates of these textures except $\{554\}\langle 225\rangle$ controlled by volume fraction become sluggish due to lower partition amount of stored energy compared with the Normal-IF steel.
4. At nucleation stage, new born γ -fibre grains mainly recrystallized in different paths: strong γ -fibre textures in the deformed Normal-IF steel would drive the rapid growth of recrystallized $\{111\}\langle 110\rangle$ grains, while significantly increased α -fibre textures in deformed RE-IF steels would provide abundant nucleation sites for γ -fibre grains and trigger competitive growth between $\{554\}\langle 225\rangle$ and $\{111\}\langle 110\rangle$ textures.
5. During grain growth and coarsening, RE elements could hardly change the intrinsic migration modes but

growth rates of different γ -fibre textures: the dominant growth texture of the Normal-IF steel transferred to $\{554\}\langle 225 \rangle$ from $\{111\}\langle 110 \rangle$, while $\{554\}\langle 225 \rangle$ textures in RE-IF steels still sustained the orientation advantage inherited from nucleation stage and kept on coarsening intensely, resulting in orientation clusters and further grain coarsening.

Acknowledgements This work was financially supported by the National Natural Science Foundation of China under Grant Nos. 52101165, 52031013, 52071322 and U1708252, the Key Research Program of the Chinese Academy of Sciences, Grant No. ZDRW-CN-2021-3 and the supporting project, Grant No. KFG-2018107. The authors express their gratitude to C.N. Tomé (Material Science and Technology Division, Los Alamos National Laboratory) for providing the VPSC code to conduct the simulations.

Declarations

Conflict of interest The authors state that there are no conflicts of interest to disclose.

References

- S. Ghosh, S. Mula, *Mater. Sci. Eng. A* **646**, 218 (2015)
- A. Haldar, R.K. Ray, *Mater. Sci. Eng. A* **391**, 402 (2005)
- B.J. Duggan, Y.Y. Tse, G. Lam, M.A. Quadir, *Mater. Manuf. Process.* **26**, 51 (2011)
- S. Ghosh, A.K. Singh, S. Mula, P. Chanda, V.V. Mahashabde, T.K. Roy, *Mater. Sci. Eng. A* **684**, 22 (2017)
- Y. Nagataki, Y. Hosoya, *ISIJ Int.* **36**, 451 (1996)
- S. Ghosh, S. Mula, *Mater. Charact.* **159**, 110003 (2020)
- M. Oyarzábal, A. Martínez-de-Guerenu, I. Gutiérrez, *Mater. Sci. Eng. A* **485**, 200 (2008)
- M. Sánchez-Araiza, S. Godet, P.J. Jacques, J.J. Jonas, *Acta Mater.* **54**, 3085 (2006)
- A. Bodin, J. Sietsman, S. Van Der Zwaag, *Metall. Mater. Trans. A* **33**, 1589 (2002)
- H. Chen, Z.B. He, L. Lu, *J. Mater. Sci. Technol.* **36**, 37 (2020)
- J. Suharto, Y.G. Ko, *Mater. Sci. Eng. A* **558**, 90 (2012)
- R. Saha, R.K. Ray, *Scr. Mater.* **57**, 841 (2007)
- L. Zhang, Z. Chen, Y.H. Wang, G.Q. Ma, T.L. Huang, G.L. Wu, D.J. Jensen, *Scr. Mater.* **141**, 111 (2017)
- S.L. Xie, Z.B. Wang, K. Lu, *J. Mater. Sci. Technol.* **35**, 460 (2019)
- A. De Paepe, J.C. Herman, P. Hekker, E.F.M. Jansen, *Rev. Metall.* **97**, 905 (2000)
- P. Juntunen, P. Karjalainen, D. Raabe, G. Bolle, T. Kopio, *Metall. Mater. Trans. A* **32**, 1989 (2001)
- W.C. Jeong, *Metall. Mater. Trans. A* **37**, 3737 (2006)
- P. Ghosh, C. Ghosh, R.K. Ray, *Acta Mater.* **58**, 3842 (2010)
- C.Y. Yang, P. Liu, Y.K. Luan, D.Z. Li, Y.Y. Li, *Int. J. Fatigue* **128**, 105193 (2019)
- H.H. Liu, P.X. Fu, H.W. Liu, Y.F. Cao, C. Sun, N.Y. Du, D.Z. Li, *J. Mater. Sci. Technol.* **50**, 245 (2020)
- D.Z. Li, P. Wang, X.Q. Chen, P.X. Fu, Y.K. Luan, X.Q. Hu, H.W. Liu, M.Y. Sun, Y. Chen, Y.F. Cao, L.G. Zheng, J.Z. Gao, Y.T. Zhou, L. Zhang, X.L. Ma, C.L. Dai, C.Y. Yang, Z.H. Jiang, Y. Liu, Y.Y. Li, *Nat. Mater.* **21**, 1137 (2022)
- R.X. Yang, X. Cai, L.G. Zheng, X.Q. Hu, D.Z. Li, *Acta Metall. Sin-Engl. Lett.* (2022). <https://doi.org/10.1007/s40195-022-01467-7>
- J.C. Yang, C.Q. Yang, X.J. Liu, Z. Jian, *Forg. Stamp. Technol.* **39**, 91 (2014)
- H. Wang, Y.P. Bao, C.Y. Duan, L. Lu, Y. Liu, Q. Zhang, *Materials* **13**, 1473 (2020)
- M. Mehdi, Y. He, E.J. Hilinski, A. Edrissy, *Metall. Mater. Trans. A* **50**, 3343 (2019)
- R. Tuttle, *Int. J. Metalcast.* **6**, 51 (2012)
- E.O. Hall (ed.), *The Deformation and Aging of Mild Steel* (1951)
- M. Mehdi, Y.L. He, E.J. Hilinski, L.A.I. Kestens, A. Edrissy, *Steel Res. Int.* **90**, 1800582 (2019)
- J.T. Park, J.A. Szpunar, *Acta Mater.* **51**, 3037 (2003)
- D. Dorner, S. Zaefferer, D. Raabe, *Acta Mater.* **55**, 2519 (2007)
- H.J. Gao, Y.G. Huang, *Scr. Mater.* **48**, 113 (2003)
- W. Oliferuk, M. Maj, *Eur. J. Mech. A-Solids* **28**, 266 (2009)
- J.F. Nye, *Acta Mater.* **1**, 153 (1953)
- W. Oliferuk, S.P. Gadaj, M.W. Grabski, *Mater. Sci. Eng. A* **70**, 131 (1985)
- G.X. Hu, Z. Cai, Y.H. Rong (eds.), *Fundamentals of Materials Science*, 3rd edn. (Shanghai Jiaotong University Press, Shanghai, 2010), pp. 172–178
- W. Oliferuk, M. Maj, *Eur. J. Mech. A-Solid* **28**, 266 (2009)
- W.M. Mao, P. Yang (ed.), *Material Science Principles on Electrical Steels*, 1st edn. (Higher Education Press, Beijing, 2013), Chapter 3.2
- C. Tome, R. Lebensohn (ed.), *Material Modeling with the Visco-Plastic Self-Consistent (VPSC) Approach-Theory and Practical Applications*, 1st edn. ISBN: 9780128207130 (2023)
- Y. Rika, T. Ichiro, I. Tsuyoshi, S. Tadashi, *ISIJ Int.* **34**, 70 (1994)
- S.S. Hazra, A.A. Gazder, E.V. Pereloma, *Mater. Sci. Eng. A* **524**, 158 (2009)
- B.J. Duggan, M.Z. Quadir, Y.Y. Tse, K. Shen, G.L. Liu, Q.Z. Chen, *Mater. Sci. Forum* **558**, 61 (2007)
- M. Mehdi, Y.L. He, E.J. Hilinski, L.A.I. Kestens, A. Edrissy, *Acta Mater.* **185**, 540 (2020)
- A. Samet-Meziou, A.L. Etter, T. Baudin, R. Penelle, *Scr. Mater.* **53**, 1001 (2005)
- S.H. Choi, *Acta Mater.* **51**, 1775 (2003)
- Y.H. Guo, Z.D. Wang, L.Q. Wei, *J. Mater. Eng. Perform.* **23**, 1214 (2014)

Springer Nature or its licensor (e.g. a society or other partner) holds exclusive rights to this article under a publishing agreement with the author(s) or other rightsholder(s); author self-archiving of the accepted manuscript version of this article is solely governed by the terms of such publishing agreement and applicable law.